

A fast-rotator post-starburst galaxy quenched by supermassive black-hole feedback at $z=3$

Francesco D'Eugenio^{1,2*‡}, Pablo G. Pérez-González^{3‡}, Roberto Maiolino^{1,2,4}, Jan Scholtz^{1,2}, Michele Perna³, Chiara Circosta^{5,4}, Hannah Übler^{1,2}, Santiago Arribas³, Torsten Böker⁶, Andrew J. Bunker⁷, Stefano Carniani⁸, Stephane Charlot⁹, Jacopo Chevallard⁷, Giovanni Cresci¹⁰, Emma Curtis-Lake¹¹, Gareth C. Jones⁷, Nimisha Kumari¹², Isabella Lamperti³, Tobias J. Looser^{1,2}, Eleonora Parlanti⁸, Hans-Walter Rix¹³, Brant Robertson¹⁴, Bruno Rodríguez Del Pino³, Sandro Tacchella^{1,2}, Giacomo Venturi⁸ and Chris J. Willott¹⁵

¹Kavli Institute for Cosmology, University of Cambridge, Madingley Road, Cambridge, CB3 0HA, UK.

²Cavendish Laboratory - Astrophysics Group, University of Cambridge, 19 JJ Thomson Avenue, Cambridge, CB3 0HE, UK.

³Centro de Astrobiología (CAB), CSIC-INTA, Ctra. de Ajalvir km 4, Torrejón de Ardoz, E-28850, Madrid, Spain.

⁴Department of Physics and Astronomy, University College London, Gower Street, London WC1E 6BT, UK.

⁵European Space Agency (ESA), European Space Astronomy Centre (ESAC), Camino Bajo del Castillo s/n, 28692 Villanueva de la Cañada, Madrid, Spain.

⁶European Space Agency, c/o STScI, 3700 San Martin Drive, Baltimore, MD 21218, USA.

⁷University of Oxford, Department of Physics, Denys Wilkinson Building, Keble Road, Oxford OX13RH, United Kingdom.

⁸Scuola Normale Superiore, Piazza dei Cavalieri 7, I-56126 Pisa, Italy.

⁹Sorbonne Université, UPMC-CNRS, UMR7095, Institut d'Astrophysique de Paris, F-75014 Paris, France.

¹⁰INAF - Osservatorio Astrofisico di Arcetri, largo E. Fermi 5, 50127 Firenze, Italy.

¹¹Centre for Astrophysics Research, Department of Physics,
Astronomy and Mathematics, University of Hertfordshire, Hatfield
AL10 9AB, UK.

¹²AURA for European Space Agency, Space Telescope Science
Institute, 3700 San Martin Drive. Baltimore, MD, 21210.

¹³Max Planck Institute for Astronomy, Königstuhl 17, 69117
Heidelberg, Germany.

¹⁴Department of Astronomy and Astrophysics University of California,
Santa Cruz, 1156 High Street, Santa Cruz CA 96054, USA.

¹⁵NRC Herzberg, 5071 West Saanich Rd, Victoria, BC V9E 2E7,
Canada.

*Corresponding author(s). E-mail(s): francesco.deugenio@gmail.com;

‡These authors contributed equally to this work.

Abstract

There is compelling evidence that the most massive galaxies in the Universe stopped forming stars due to the time-integrated feedback from their central super-massive black holes (SMBHs). However, the exact quenching mechanism is not yet understood, because local massive galaxies were quenched billions of years ago. We present *JWST*/NIRSpec integral-field spectroscopy observations of GS-10578, a massive, quiescent galaxy at redshift $z = 3.064$. From the spectrum we infer that the galaxy has a stellar mass of $M_{\star} = 1.6 \pm 0.2 \times 10^{11} M_{\odot}$ and a dynamical mass $M_{\text{dyn}} = 2.0 \pm 0.5 \times 10^{11} M_{\odot}$. Half of its stellar mass formed at $z = 3.7\text{--}4.6$, and the system is now quiescent, with the current star-formation rate $\text{SFR} < 9 M_{\odot} \text{ yr}^{-1}$. We detect ionised- and neutral-gas outflows traced by [O III] emission and Na I absorption. Outflow velocities reach $v_{\text{out}} \approx 1,000 \text{ km s}^{-1}$, comparable to the galaxy escape velocity and too high to be explained by star formation alone. GS-10578 hosts an Active Galactic Nucleus (AGN), evidence that these outflows are due to SMBH feedback. The outflow rates are $0.14\text{--}2.9$ and $30\text{--}300 M_{\odot} \text{ yr}^{-1}$ for the ionised and neutral phases, respectively. The neutral outflow rate is ten times higher than the SFR, hence this is direct evidence for ejective SMBH feedback, with mass-loading capable of interrupting star formation by rapidly removing its fuel. Stellar kinematics show ordered rotation, with spin parameter $\lambda_{\text{Re}} = 0.62 \pm 0.07$, meaning GS-10578 is rotation supported. This study shows direct evidence for ejective AGN feedback in a massive, recently quenched galaxy, thus clarifying how SMBHs quench their hosts. Quenching can occur without destroying the stellar disc.

The Universe today is not what it used to be [1]. Local, massive quiescent galaxies stand like colossal wrecks of glorious but remote star-formation histories, and mighty and rapid quenching the likes of which have no present-day equals [2, 3].

JWST enables us for the first time to witness these monumental galaxies during the long-gone epoch when they arose and fell. By redshift $z = 1.5$ – 2 , 3–4 Gyr after the Big Bang, massive quiescent galaxies have little to no cold gas, the fuel for star formation [4, 5]. But the question whether the missing fuel was consumed by starbursts or if it was removed by ‘ejective’ feedback from SMBHs remains open [6, 7]. We present a NIRSpec/IFS impression of GS-10578, a massive, quiescent galaxy at redshift $z = 3.064$ (look-back time 11.7 Gyr). Observed as part of the Galaxy Assembly with NIRSpec Integral Field Spectroscopy GTO programme (GA-NIFS), this galaxy (Fig. 1a) was selected as a ‘blue nugget’ [8], a class of massive, extremely compact galaxies (stellar mass $M_{\star} = 3$ – $30 \times 10^{10} M_{\odot}$, half-light radius $R_e = 0.5$ – 2 kpc), thought to be the progenitors of compact quiescent galaxies at $z = 2$ (‘red nuggets’, [9]). Blue nuggets are believed to be undergoing ‘gas-rich compaction’, that is, a central starburst driven by disc instability or gas-rich major mergers, followed by rapid quenching [10] and leaving a compact, quiescent red-nugget galaxy. As we will show, GS-10578 is instead already a red nugget in an advanced stage of quenching. The system is merging with multiple low-mass satellites and is undergoing powerful, ejective feedback from its SMBH.

NIRCam imaging [11–13] reveals a system with several smaller companions, all within 8 kpc in projection (labelled GS-10578b–f in Fig. 1a, of which GS-10578b–d are spectroscopically confirmed to be satellites). Multiple low-mass satellites are a common occurrence for massive quiescent galaxies at high redshift [14]. GS-10578 shows a regular, elliptical shape at 2.77–4.44 μm , but the light distribution is increasingly lopsided blueward of 2 μm (Fig. 1b), with the brightest region at 0.9 μm clearly offset to the north west (by 0.5 kpc) and displaying two peaks.

We use the NIRSpec/IFS data with the low-resolution prism disperser to perform spaxel-by-spaxel full spectral energy distribution (SED) modelling, to measure the surface stellar mass density, spatially resolved stellar population properties and star-formation history (SFH; see Methods). The resulting mass distribution is symmetric, with no strong signs of asymmetry (Fig. 2a). The asymmetric light distribution at rest-frame UV wavelengths arises from younger stellar populations (luminous but with low stellar mass), and/or from an asymmetric dust distribution. Integrating the 2-d properties inside a circular aperture of 1.2 arcsec radius, and correcting for aperture losses, we measure a total stellar mass $M_{\star} = 1.6 \pm 0.2 \times 10^{11} M_{\odot}$ (surviving stellar mass). The total SFH from all spaxels shows that the main star-formation episode happened at $z = 3.7$ – 4.6 , 0.4–0.8 Gyr prior to observation. Afterwards, the star-formation rate (SFR) rapidly declined. There is some evidence of a recent upturn, but our models do not include an Active Galactic Nucleus (AGN), therefore this upturn could be due to the nebular emission being interpreted as due to star formation. The SFR averaged over the last 100 Myr, is $40 \pm 20 M_{\odot} \text{ yr}^{-1}$. This is five times below the star-forming main sequence at $z = 3$ [15], and comparable to the quiescence threshold of $19 M_{\odot} \text{ yr}^{-1}$ [16]. However, part of the SFR is likely due to the satellites, and the nebular emission is mostly powered by the AGN, meaning that the true SFR is likely much lower. This implies that GS-10578 is currently quenched and on its way to quiescence, which is consistent with the empirical UVJ-colour diagnostic [17], and with the SFR inferred from the emission-line analysis.

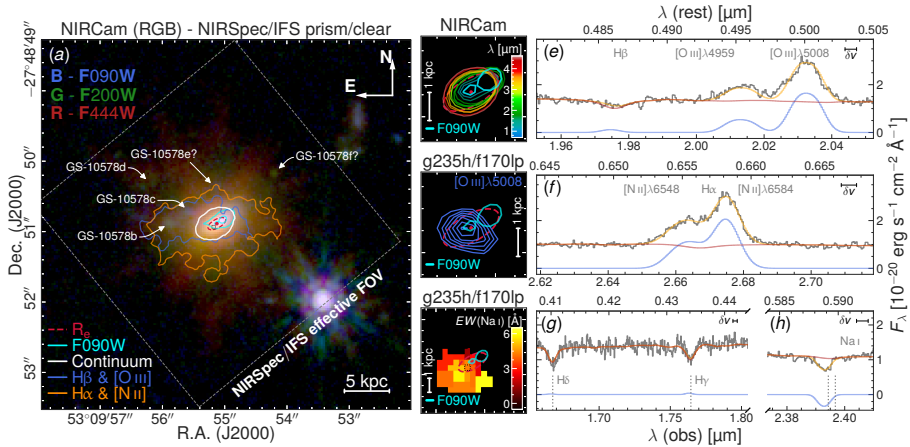


Fig. 1: Panel a. False-colour image of GS-10578 from NIRCcam. The grey dashed square is the field of view of NIRSpect/IFS (with dithering). The solid white contour is a stellar isophote from NIRSpect/IFS prism spectroscopy, the red dashed ellipse is the best-fit deconvolved model, with semi-major axis equal to $1 R_e$. The cyan contours are rest-frame UV from NIRCcam F090W, displaying complex morphology, probably due to foreground dust. The orange/blue contours are isosignificance lines for the H α -[N II] and H β -[O III] blended lines, from the prism data. The nebular emission is significantly more extended than the stellar light, indicating the ability of mergers/feedback to enrich the circum-galactic medium (CGM). **Panel b.** Comparing the model isophote (red dashed ellipse) to NIRCcam isophote morphology, there is a clear wavelength-dependent offset to the north west. **Panel c.** Brightest [O III] emission from g235h/f170lp data, showing a slight offset from the centre of the stellar emission (cf. red dot, distance < 1 spaxel) and a remarkably different position angle, almost $\pi/2$ compared the stars. **Panel d.** Neutral gas Na I absorption, which is clearly asymmetric and located where the rest-UV photometry is faintest. **Panels e-h.** Spectrum from the dotted black spaxel highlighted in panels a and d, showing the data (grey), best-fit continuum and nebular-line model (red and blue, respectively) and the best-fit model (orange); the horizontal bar in the top right corner of each panel is $\delta v = 500 \text{ km s}^{-1}$. Panels e and f show the complex, multi-component emission-line profile of [O III] and H α -[N II]. Panels g and h show the same spaxel. The vertical dotted lines mark the position of the stellar H δ , H γ and Na I-doublet absorption; the deep Na I absorption, blueshifted with respect to the stars, betrays the presence of a neutral-gas outflow.

The NIRSpect/IFS observation in the low spectral-resolution configuration reveals extended nebular emission in both the H β -[O III] and H α -[N II] spectrally blended complexes (Fig. 1a). This nebular emission is elongated in a different direction compared to the stellar major axis, but in the same direction as GS-10578b, which suggests that the ionised gas comes from inter-stellar medium (ISM) material stripped

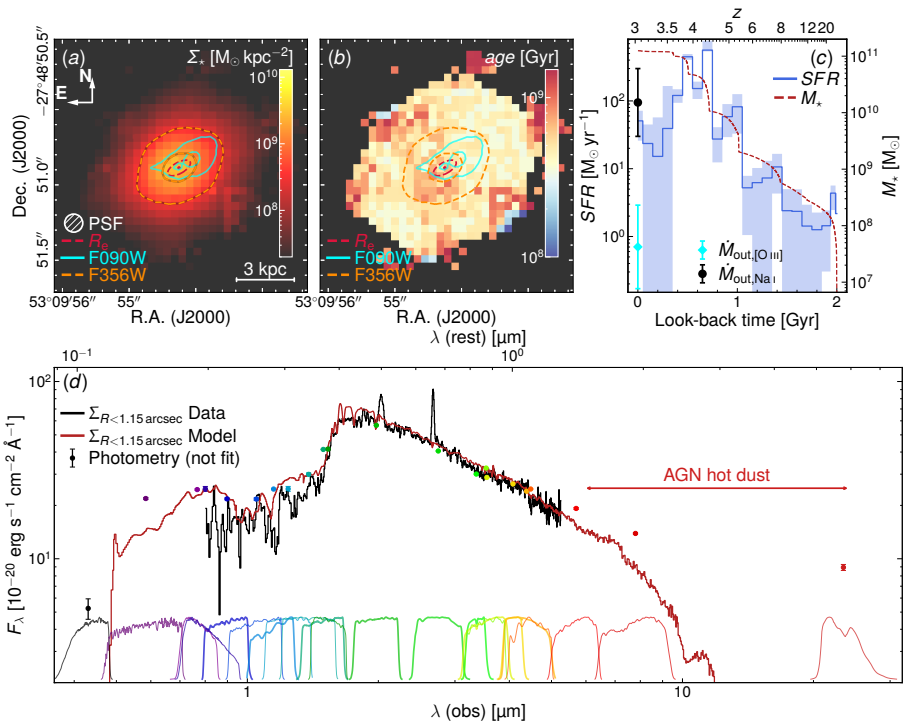


Fig. 2: Panels a–b. Stellar-population surface mass-density and mass-weighted age maps from full spectral fitting of the low-resolution spectroscopy data, showing that most of GS-10578 consists of 0.5-Gyr-old stars. Merging satellites have lower mass-to-light ratios than the GS-10578, and do not contribute to the mass-weighted properties. **Panel c.** The star-formation history from the same models, integrated over the 2-d map, shows the main episode of star formation occurred 0.5 Gyr ago. The shaded region is the 1- σ uncertainty. The cyan diamond and black circle are the mass outflow rates from $[\text{O III}]$ and Na I , respectively. Unlike the ionised-gas outflow, the neutral-gas outflow has mass loading high enough to stop star formation. **Panel d.** SED of the individual spaxels summed inside a circular aperture of radius 1.15 arcsec, for both the NIRSpec/IFS data (black) and the best-fit model (red). We also show the aperture photometry as errorbars. The model does not include an AGN, therefore it does not capture the emission lines or the flux redder than $6 \mu\text{m}$, which is dominated by host-dust emission from the AGN torus.

by the interaction with the satellite. An outflow origin is also possible, but in this case, the alignment with the satellite would be a coincidence.

Unlike the low-resolution observations, NIRSpec high-resolution data (Fig. 1b–c and e–f) are able to separate $\text{H}\alpha$ from $[\text{N II}]$, and $\text{H}\beta$ (which in GS-10578 we observe mostly in absorption) from $[\text{O III}]$. The emission lines show a broad, multi-component profile, indicating complex kinematics. The BPT diagnostic diagram (Fig. 3) shows

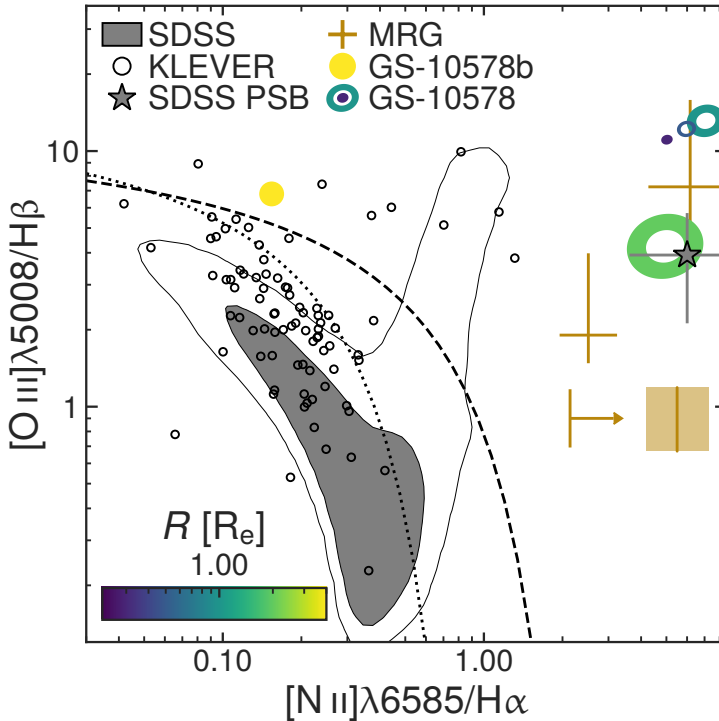


Fig. 3: Emission-line diagnostic diagram for GS-10578 compared to selected samples from the literature; the line ratios of our target place its ionisation source firmly beyond the range that can be explained by star formation (dashed line, [18]). For the main target, we show the emission-line ratios from spectra integrated inside elliptical apertures (colour coded by the semi-major axis of the aperture). The yellow circle is the eastern satellite. We show a number of samples for comparison: the contours and the small empty circles trace the distribution of galaxies at $z = 0.1$ (from SDSS) and $z = 2$ (from KLEVER, [19]), respectively. The sand symbols and upper limits are the MRG sample of post-starburst galaxies at $z = 1-2$ [20], while the grey star is one of the most extreme post-starburst galaxies in SDSS. The extreme values we find for GS-10578 are similar to what is found for other post-starburst galaxies.

that GS-10578 has everywhere a high $[N II]/H\alpha$ ratio (emission-line ratios are measured inside concentric elliptical annuli, following the shape and position angle of the stellar isophotes). From the outmost to the innermost annulus around GS-10578, $[O III]\lambda 5007/H\beta$ increases from 4 to 10, whereas $[N II]\lambda 6584/H\alpha$ remains approximately constant at 5–8. All annuli are in the AGN region of the diagram, well beyond the demarcation curve between starburst-driven and AGN-driven photoionisation [18]; moreover, all annuli lie far outside the 99th percentile of the distribution of local galaxies and AGN (grey and black contours). Star-forming and AGN galaxies at $z = 2$ also have much smaller $[N II]\lambda 6584/H\alpha$ ratios (empty circles), but we find our values to be similar to post-starburst galaxies (PSB) at $z = 1-2.5$ [21] and to

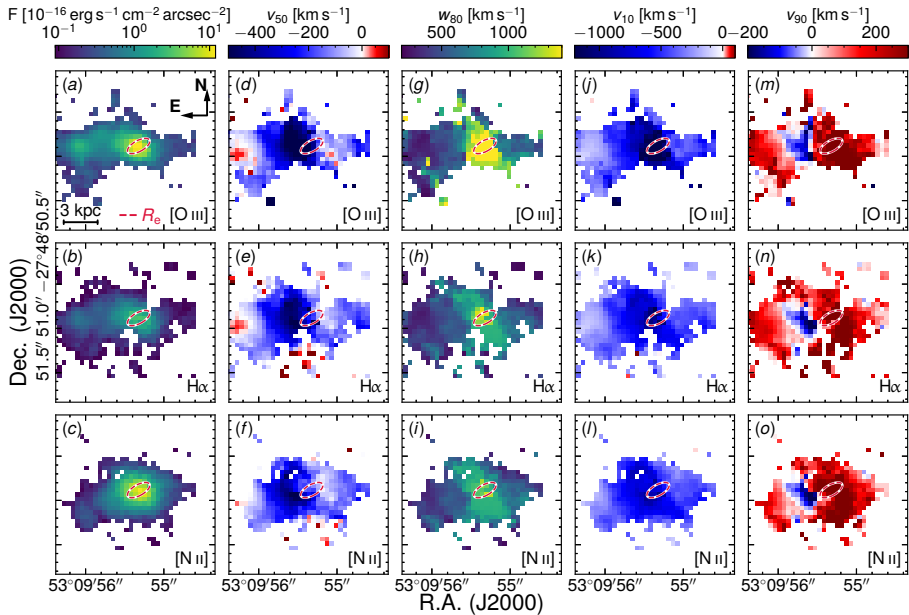


Fig. 4: Flux and kinematic maps of the $[\text{O III}]\lambda\lambda 4960,5008$, $\text{H}\alpha$ and $[\text{N II}]\lambda\lambda 6550,6585$ nebular lines. The three rows show $[\text{O III}]\lambda\lambda 4960,5008$ (top), $\text{H}\alpha$ (middle) and $[\text{N II}]\lambda\lambda 6550,6585$ (bottom). **Panels a–c.** Flux maps, obtained fitting one or two Gaussians to the emission lines (see Methods). **Panels d–f.** Non-parametric median velocity. **Panels g–i.** Inter-percentile line width. **Panels j–k.** 10th percentile velocity. **Panels l–n.** 90th percentile velocity. For GS-10578 (whose continuum emission is highlighted by the red dashed ellipse), most of the emission is in a broad, blue-shifted component. Together with information from the BPT diagram (Fig. 3), this is evidence for an AGN-powered outflow.

the most extreme PSBs in the local Universe (grey star). Assuming all $\text{H}\alpha$ emission was due to star formation, the extinction-corrected SFR on timescales of 3–10 Myr is $9 M_{\odot} \text{ yr}^{-1}$ (inside $2 R_e$, where $R_e = 1.1 \text{ kpc}$ from [22]). Varying the aperture size, the SFR ranges between $4 M_{\odot} \text{ yr}^{-1}$ (inside $1 R_e$) to $19 M_{\odot} \text{ yr}^{-1}$ (summing over the entire map, including the satellites). These values are similar to the result from the SED analysis. However, as we have seen, $\text{H}\alpha$ is dominated by emission from the AGN, therefore the true SFR is likely much lower, and we treat all these values as upper limits within their apertures. Overall, the low $\text{H}\alpha$ SFR values are in agreement with the quiescent interpretation. In addition to the BPT diagram, direct evidence for an AGN comes from the X-ray detection ($L_X = 8 \times 10^{44} \text{ erg s}^{-1}$ [23]) and from the SED excess at MIR wavelengths, which can be explained by the presence of a dusty torus around the accreting SMBH (Fig. 2d, cf. model and photometry at $24 \mu\text{m}$). Modelling the photometry using both stellar and AGN emission models gives an AGN bolometric luminosity $L_{\text{AGN}} = 2.6 \pm 0.9 \times 10^{45} \text{ erg s}^{-1}$ (see Methods; [24]).

Spatially resolved emission-line kinematics (Fig. 4) display line broadening in excess of 500 km s^{-1} , and centroids that are blueshifted relative to the stellar absorption (the stellar distribution is traced by the red dashed ellipse in Fig. 4). Most of the nebular flux comes from the central regions, but is offset from the centre of the stellar emission and is elongated almost at right angle compared to the stellar isophote (Fig. 1c). We also see a clear kinematic transition between this bright central region and the more diffuse emission at larger radii. The central region has velocity offset of -400 km s^{-1} , while the extended emission is at velocities of $\pm 100 \text{ km s}^{-1}$. Furthermore, the central regions have inter-percentile line widths w_{80} in excess of $1,000 \text{ km s}^{-1}$. The extent and elongation of the diffuse nebular emission suggest a merger origin, but most of the flux is likely associated with the blueshifted component which we interpret as an outflow. The large velocity offset and velocity width of the nebular lines – and the fact that the contours of highest flux are directed along the galaxy minor axis (Fig. 1c and Fig. 4a–c) – are evidence for an outflow normal to the disc [25, 26]. The fast outflow velocity, the low SFR, and the AGN are evidence for SMBH-feedback driven outflows [27–29]. We estimate a mass outflow rate $\dot{M}_{\text{out}}^{[\text{O III}]} = 0.14\text{--}2.9 M_{\odot} \text{ yr}^{-1}$ (see Methods), meaning the ionised-gas outflow is much lower than the SFR (Fig. 2c).

What sets GS-10578 apart from other high-redshift sources, however, is the clear detection of spatially resolved, deep absorption features. These include the prominent hydrogen absorption lines characteristic of 0.5-Gyr-old stellar populations (equivalent width $\text{EW H}\delta_{\text{A}} = 6.6\text{--}8.1 \text{ \AA}$ and $\text{H}\gamma_{\text{A}} = 4.1\text{--}6.8 \text{ \AA}$; Figs. 1g and 5e–5f) and Na I resonant absorption (Fig. 1h). The Balmer absorption confirms the results of the SED analysis (which is based on spectroscopy with much lower spectral resolution). The Na I absorption is offset both spatially and kinematically from the stars, therefore we rule out a stellar origin. The highest Na I EW translates into a column density of $6 \times 10^{22} \text{ cm}^{-2}$, ten times lower than the column density towards the X-ray AGN ($6 \times 10^{23} \text{ cm}^{-2}$, [24]). The Na I EW maps (Fig. 1d) show that the absorption extends from the centre of the galaxy to the south-east, avoiding completely the north-western half, where we detect the brightest rest-UV emission. This fact, combined with the blueshifted line-of-sight velocities ($v_{\text{Na I}} = -(250\text{--}350) \text{ km s}^{-1}$), indicate that the absorption is due to a neutral gas outflow, with a cone-like geometry possibly tilted with respect to the stellar disc. We estimate the disc inclination from the best-fit Sérsic model of [22], which gives a projected axis ratio $q = 0.44$ (we assume an intrinsic axis ratio $q_0 = 0.2$). After correcting for inclination by a factor $\cos i$, we obtain an outflow velocity of order $-1,000 \text{ km s}^{-1}$ – again too fast to be explained by star formation alone. Assuming a maximal escape velocity of $v_{\text{esc}} = 1,200 \text{ km s}^{-1}$, we infer a velocity ratio $v_{\text{Na I}}/v_{\text{esc}} = 0.8 \pm 0.2$, meaning the outflows are certainly capable of removing material from the star-forming disc, with a fraction possibly escaping the galaxy altogether.

We assume an outflow extent $R_{\text{out}} = 2.7 \text{ kpc}$, based on the largest distance between the Na I detection and the centre of the galaxy. With this R_{out} and a thin-shell geometry, the mass outflow rate is $\dot{M}_{\text{out}}^{\text{Na I}} \approx 100 M_{\odot} \text{ yr}^{-1}$, with uncertainties of a factor

of 3. This value is larger than the SFR – particularly if we recall that the SFR is overestimated (Fig. 2c). This indicates that the neutral-gas outflow is capable of halting star formation by removing the necessary fuel.

In Fig. 5 we show the stellar kinematics of GS-10578. We measure a clear velocity gradient between the east and west sides (cf. Fig. 5e and f). Could this gradient be due to a major merger? In favour of this hypothesis, the two sides of GS-10578 have different continuum shapes, with the south-east side (panel e) displaying flatter continuum slope and broader, less deep absorption. Rest-frame UV photometry shows multiple peaks, and the stellar velocity-dispersion σ_* is highest in the south east, rather than at the centre of the galaxy. However, contrary to the merger expectation, both UV peaks are located on the same (receding) region of the velocity map (cyan contours in Fig. 5d), therefore these two peaks are unlikely to trace two distinct galaxies merging. In case of a merger, σ_* would be highest between the two galaxies, where absorption lines of different redshift blend. Moreover, the mass maps and the red-wavelength NIRC*am* imaging show an elliptical morphology centred at – or very near – the kinematic centre of the maps, which is also in contrast with the merger hypothesis (Fig. 2a, and orange contours in Fig. 5d, see also Figs. 1b). Finally, the putative rotation axis is aligned with the minor axis of the isophotes (and isodensity contours), as expected from regular rotation. Under the rotation hypothesis, the different spectral shapes between the receding and approaching halves of the velocity map could be due to a combination of more dust in the south east (where we also detect the neutral-gas outflow, Figs. 1d and 5c), a slightly younger stellar population in the north west (Fig. 2b), and stronger absorption-line infill due to nebular emission in the south east. Most likely, all three factors contribute to the observed spectral differences.

By applying the virial theorem to the aperture velocity dispersion inside $1 R_e$, $\sigma_{\star,e} = 356 \pm 36 \text{ km s}^{-1}$, we find a dynamical mass of $M_{\text{dyn}} = 2.0 \pm 0.5 \times 10^{11} M_\odot$ (using the calibration of [30]), which is comparable to M_\star . In case of a major merger, both $\sigma_{\star,e}$ and R_e would be severely overestimated, meaning the true M_{dyn} would be much lower than what inferred from the virial theorem, in tension with M_\star . Based on all this evidence, we classify GS-10578 as a regular (fast) rotator – the most distant yet found from stellar kinematics. An alternative possibility, is that GS-10578 is a system in an advanced stage of merger, with the orbital angular momentum of the two progenitors locked in the stars [31]. To measure the degree of rotation support, we use the λ_{R_e} spin parameter, a proxy for the angular momentum per unit mass [32], defined by

$$\lambda_{R_e} \equiv \frac{\sum_{r < R_e} F_i r_i |v_i|}{\sum_{r < R_e} F_i r_i \sqrt{v_i^2 + \sigma_i^2}} \quad (1)$$

where we calculate the radius r_i of each spatial element along the best-fit ellipse [33], the aperture is the observed isophote of semi-major axis one R_e , F_i is the continuum flux, and v_i and σ_i are the stellar velocity and velocity dispersion. We measure $\lambda_{R_e}(\text{observed}) = 0.46$, then apply a model-based point-spread function (PSF) correction (dependent on the galaxy size and light profile [34]) for a Gaussian PSF with full width at half maximum FWHM=0.09 arcsec, obtaining $\lambda_{R_e} = 0.62 \pm 0.07$ (the uncertainties include the uncertainties due to the correction).

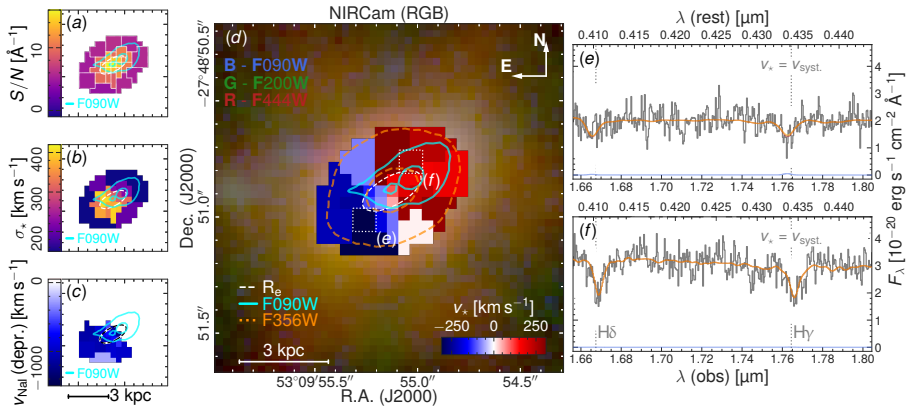


Fig. 5: Panels a–d. Voronoi-binned 2-d maps of GS-10578, showing the empirical S/N (panel a), stellar velocity v_* (panel d), instrument-deconvolved velocity dispersion σ_* (panel b) and neutral-gas velocity v_{NaI} (panel c). In these four panels the dashed ellipse traces the shape and R_e of the best-fit Sérsic model to the stellar continuum. Panel a also shows the contours of the Voronoi bins (white dotted lines). Panel d shows an enlarged region of the RGB image from Fig. 1a in the background, for comparison. Panel d shows clear evidence for ordered rotation, with the rotation axis along the minor axis of the stellar distribution. **Panels e–f.** Detail on the H δ and H γ stellar absorption features from two Voronoi bins (white dotted squares in panel d), chosen to highlight the velocity offset that we attribute to stellar rotation. The line colours are the same as Fig. 1e–h.

In Fig. 6a we compare GS-10578 to other quiescent galaxies. Based on its location on the λ_{R_e} - ϵ plane (where ϵ is the ellipticity of the isophote at $1 R_e$), GS-10578 is a clear fast-rotator (FR) galaxy [32], i.e., it is consistent with being an oblate spheroid with mild anisotropy, dominated by rotation support. FRs are rare among galaxies of similar mass in the local Universe [35, 36], but were much more common at high redshifts[21]. Fig. 6b shows GS-10578 on the mass-size plane: its compact size would again make it a strong outlier at $z = 0$ and even possibly at $z = 2$. Taken together, Figs. 6a and b imply that galaxies like GS-10578 must undergo significant dynamical and morphological evolution between $z = 3$ and present. This evolution has to decrease the angular momentum and increase the size – all while not exceeding the stellar mass of local massive galaxies. It has been postulated that this kind of growth can only be achieved via gas-poor minor mergers [37, 38], because gas-rich merger trigger starbursts and disc (re-)formation – which would increase the light-weighted λ_{R_e} parameter [39, 40]. Our target is surrounded by three and up to five faint, low-mass satellites, which may represent the fuel for the postulated size growth [14].

GS-10578 represents a unique opportunity to study how the most massive galaxies in the Universe became – and stayed – quiescent. Even though we cannot draw general conclusions from a single target, we show that AGN feedback is capable of

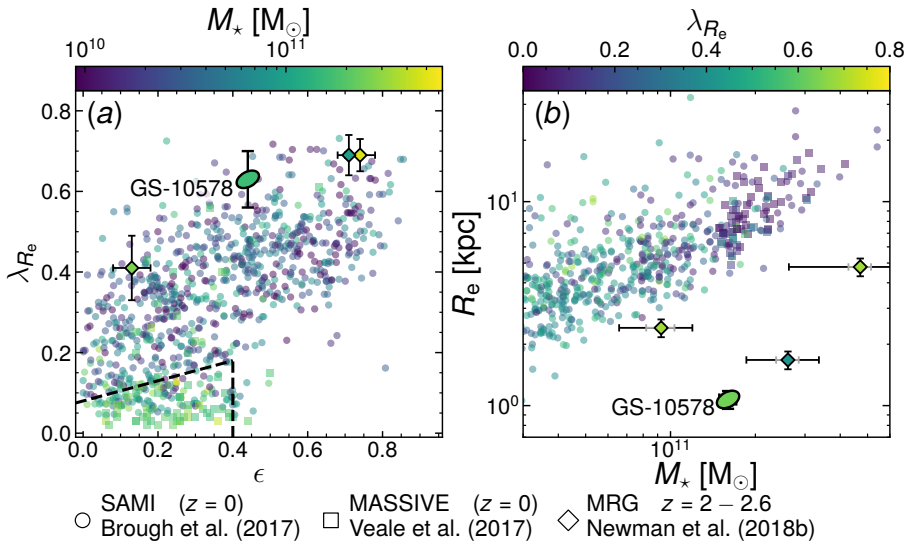


Fig. 6: Panel a. λ_{R_c} – ϵ diagram showing that – interpreting the velocity field as stellar rotation – GS-10578 is rotation supported, a so-called fast-rotator galaxy (slow rotators fall inside or near the dashed box, [41]). This is similar to other quiescent galaxies at high redshift (MRG sample, diamonds; [21]) and unlike local quiescent galaxies (SAMI sample, circles; [33]), including the most massive local quiescent galaxies (MASSIVE sample, squares; [42]). **Panel b.** Mass–size diagram, illustrating that GS-10578 is extremely compact; to join the $z = 0$ distribution, our galaxy must grow in size by a factor of 10.

powering neutral-gas outflows with high velocity and high mass loading, sufficient to interrupt star formation by removing its cold-gas fuel. In contrast, the ionised-gas outflows appear to have much lower mass loading and may be ineffective at halting star formation, in agreement with studies of other AGNs at high redshift. It is unclear how much cold gas an AGN like the one active in GS-10578 may leave behind. Non-detection from existing sub-mm observations of CO emission give a molecular-gas mass fraction $f < 10$ per cent [24], lower than the value of coeval star-forming galaxies [43], but not sufficiently constraining. Current evidence from redshifts $z = 1.5$ – 2 suggests that quiescent galaxies have low (3 per cent) molecular-gas fractions [4, 5] – an order of magnitude lower than coeval star-forming galaxies. Any leftover gas may have low star-forming efficiency, perhaps due to stabilisation against gravitational collapse and/or (AGN-induced) turbulence, similar to local PSB galaxies [44] and AGN hosts [45]. The ISM/CGM around GS-10578 suggest that a combination of AGN feedback and mergers may be providing the energy required to sustain this turbulence against dissipation. The presence of a stellar disc suggests that feedback was ‘gentle’ enough to preserve the dynamical structure of GS-10578 throughout its quenching phase, therefore dynamical transformation from disc-like

FRs to spheroid-like SRs happens after quenching. A census of the emission-line properties of high-redshift, massive quiescent galaxies is essential to clarify if strong, ejective SMBH feedback is episodic or if it is a key mechanism for driving and maintaining quiescence.

1 Methods

1.1 NIRSpec observations and data reduction

Our observations are part of the GA-NIFS survey, a large NIRSpec GTO survey targeting extended galaxies and AGNs at $z > 3$ with the NIRSpec Integral Field Spectroscopy (IFS, [46]) mode (PIs: S. Arribas, R. Maiolino). Data for GS-10578 was obtained from programme PID 1216 (PI: N. Lützgendorf) and consist of two disperser/filter combinations. Observations with the prism/clear setup cover the full wavelength range of NIRSpec with spectral resolution $R = 30\text{--}300$ [47], whereas the g235h/f170lp observations probe only 1.66–3.17 μm but with higher resolution $R = 2,700$. Both observations had a *JWST* position angle of -99° , resulting in a NIRSpec position angle of 39.5° (measured north to east). For prism/clear we used the IRS2RAPID readout pattern, 33 groups per integration and 8 exposures, for a total of 1.1 h on source; for g235h/f170lp we used the IRS2 readout pattern, 25 groups per integration and 8 exposures, for a total of 4.1 h on source. The exposures were dithered following the medium cycling pattern to improve the PSF sampling and to marginalise against detector defects and leakage/open shutters from the NIRSpec Micro-Shutter Assembly.

For the data reduction, we follow the procedure described in [48]; here we report a brief summary and highlight any differences. We reduced the data with the publicly available *jwst* pipeline, version 1.8.2, using static calibrations from the context file version 1014 (for g235h/f170lp) and context file version 1068 (for prism/clear). The pipeline was patched to include a number of corrections and improvements, as described in [48]. Compared to the default reduction, we used an additional correction for the $1/f$ noise. For g235h/f170lp, flux calibration was done in post-processing using data from the standard star TYC 4433-1800-1 (PID 1128, observation 9). To detect and flag outliers we used a custom algorithm, similar to [49]. Their algorithm was developed specifically for (spatially) undersampled *HST* images. However, NIRSpec/IFS data is undersampled only in the spatial direction, therefore we calculated the derivative of the count-rate maps only along the detector x axis, which is the approximate direction of the dispersion axis (the trace curvature can be neglected on scales of two detector pixels). The absolute value of the derivative was then normalised by the local flux (or by $3\times$ the noise, whichever was highest) and we rejected pixels where the normalised derivative was higher than the 95th-percentile of the resulting distribution. For the cube-building stage, we used the drizzle algorithm to produce cubes with a scale of 0.05 arcsec per spaxel, for both the prism/clear and the g235h/f170lp datacubes. For the PSF modelling (Method III), we used a cube with 0.03 arcsec per spaxel.

We use publicly available photometry for additional flux calibration (see S 1.4). At wavelengths 0.4–1.6 μm we use *HST*/ACS data from GOODS [50, 51] and

HST/WFC3 IR data from CANDELS [52, 53]; at wavelengths 0.9–4.8 μm we use *JWST*/NIRCam data from the *JWST* Advanced Deep Extragalactic Survey (JADES; PID 1180, PI: D. J. Eisenstein; [11, 12]) and from the *JWST* Extragalactic Medium-band Survey JEMS (PID 1963, PIs: C. C. Williams, S. Tacchella and M. Maseda; [13]).

1.2 Point-spread function determination

We present three independent measurements of the shape and size of the NIRSpec/IFS PSF. The first measurement uses observations of a standard star with the g235h/f170lp grating/filter combination. The second method uses a serendipitous star inside the NIRSpec/IFS field of view of GS-10578. The third method uses NIRCam imaging from the JADES and JEMS surveys (for which the PSF is well understood) to infer the NIRSpec/IFS PSF.

Method I – Standard star observations. We used the standard star TYC 4433-1800-1 ($V_3=188^\circ$, $PA=146.5^\circ$), reduced using the same pipeline and context file as the galaxy data, and modelled the PSF using the multi-Gaussian expansion algorithm MGEFIT [MGE; 54]. We divide the datacube in one hundred wavelength intervals between 1.66–3.17 μm , then find the PSF position angle from the second moment of the light distribution, and the best-fit MGE model by minimising χ^2 . The formal flux uncertainties on the wavelength-collapsed datacube are very small, and likely dominated by systematic uncertainties. Our χ^2 -minimisation uses therefore flux weighting instead of error weighting. The resulting FWHM is shown in Fig 7a; filled and empty stars are the model FWHM along the major and minor axis of the PSF, respectively; the solid lines are the running median (note the detector gap at 2.5 μm). In panel b the solid line is the position angle of the PSF with respect to the NIRSpec position angle; a value of 0° indicates that the PSF major axis has the same direction as the slices long axes (hereafter: along slices; 90° is across slices). We find the NIRSpec/IFS PSF to be preferentially aligned close to along slices. At short wavelengths, the PSF is larger than the NIRCam PSF (coloured dots), and there seems to be a drop in FWHM around 3 μm .

Method II – Serendipitous Star. For this method, we use the relatively bright star inside the NIRSpec field of view (Fig. 1a; $F_{775W} = 25$ mag), modelled as a Gaussian. The prism/clear datacube for GS-10578 is summed over six wavelength elements, and each synthetic image is fit independently. We then model the resulting FWHM as a function of wavelength with the function:

$$FWHM(\lambda) = (0.13 + 1.6 \cdot \lambda[\mu\text{m}]) \cdot \exp(-21.4/\lambda[\mu\text{m}]) \text{ arcsec} \quad (2)$$

This model is shown as a dot-dashed grey line in Fig. 7a; we remark that this determination may suffer from edge effects – particularly at the longest wavelengths.

Method III – Matching NIRCam imaging. For this method, we select a NIRCam wide- or medium-band filter, integrate the NIRSpec/IFS prism/clear cube (0.03 arcsec/spaxel) under the filter transmission curve to create a synthetic image in that band, then proceed to find the kernel convolution that best matches the available NIRCam image to the synthetic NIRSpec image. The NIRSpec/IFS PSF is

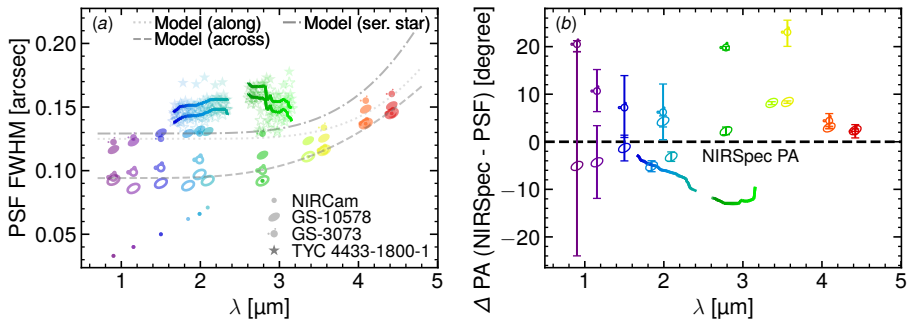


Fig. 7: Panel a. NIRSpec PSF as a function of wavelength, using three methods. Method I (stars and solid lines) uses the calibration star TYC 4433-1800-1. Method II (dot-dashed line) uses the serendipitous star inside the NIRSpec/IFS field of view for the observations of GS-10578. Method III uses NIRCcam wide- and medium-band imaging to model the PSF with a 2-d Gaussian with orthogonal axes, with one axis closer to the slice direction (filled symbols) and one closer to across slices (empty symbols). The dots show the FWHM of the NIRCcam empirical PSF for comparison. **Panel b.** Position angle of the PSF major axis (points with error bars) compared to the NIRSpec position angle (dashed horizontal line). The major axis of the PSF is closer to the direction of the slices.

then estimated as the convolution of the NIRCcam PSF with the best-fit kernel. The model consists of six free parameters; the kernel is assumed to be a pixel-integrated, bivariate Gaussian, with three free parameters σ , axis ratio q and position angle. In addition, we allow a small pixel adjustment to align the NIRCcam and NIRSpec images and a flux scaling factor. The model is optimised using the Markov-Chain Monte-Carlo algorithm `emcee` [55]. We use flat priors for the kernel parameters ($0.003 < \sigma < 0.5$ arcsec, $-90 < \text{position angle} < 90^\circ$ and $0 < q < 1$) and informative, Gaussian priors for matching the NIRCcam image position and flux (the pixel shifts are Gaussians with mean 0 and standard deviation three pixels, and the flux scaling factor is a Gaussian with mean equal to the mean flux ratio and standard deviation of 10 per cent). An example posterior distribution is shown in Fig. 8, which shows that – as for Method I above – the PSF is not circular. Fig. 7a shows the results from method III as coloured ellipses, with the filled and empty symbols denoting the PSF FWHM along the major and minor axes of the PSF, respectively. The position angle is once again close to 0, i.e., the PSF tends to be aligned with the IFS slices (panel b). This method also finds a drop in the PSF FWHM between the NIRCcam F210M and F277W filters; the origin of this drop is unclear and we do not model it in the subsequent analysis. We tested that our results are consistent when modelling the convolution kernel as a superposition of two Gaussians with the same axis ratio and position angle. In addition to GS-10578, we also model GS-3073, a AGN-host galaxy at $z = 5.55$ [56]. The results are shown by the GS-3073-shaped markers, with filled and empty symbols having the same meaning as for GS-10578. Using both GS-10578 and GS-3073, we model the PSF FWHM along the major axis (i.e., along

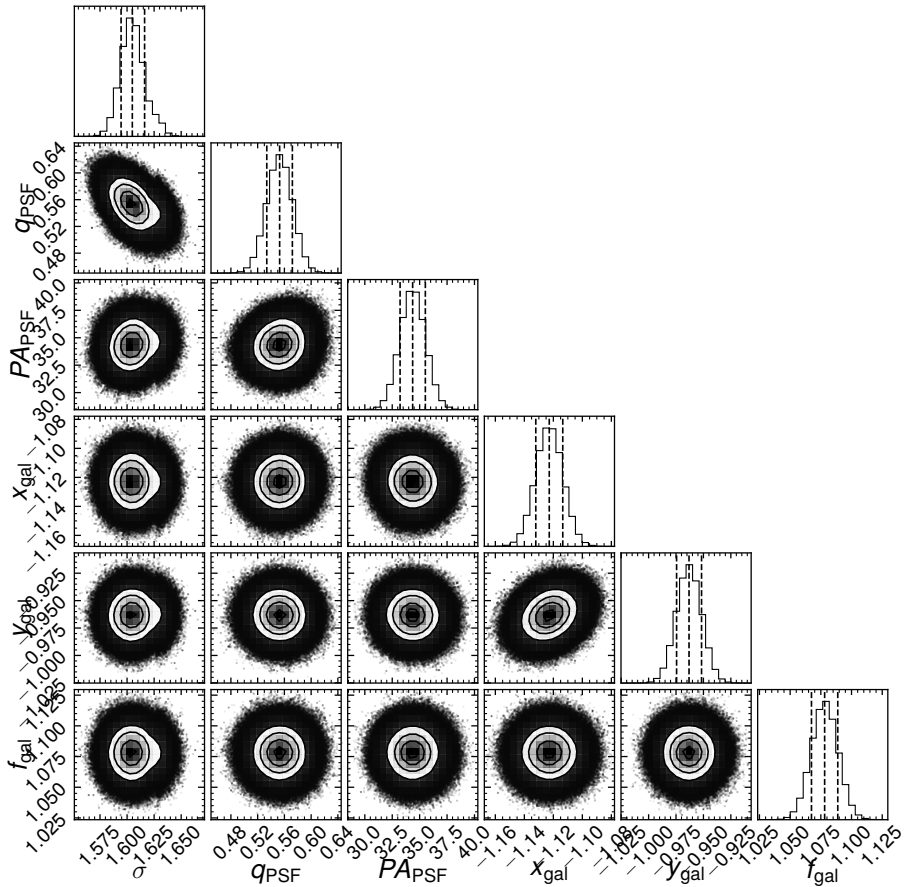


Fig. 8: Example posterior distribution for our PSF estimation based on matching NIRCcam imaging to synthetic NIRCspec/IFS imaging (method II). σ is the semi-major axis standard deviation of the Gaussian kernel we apply to the NIRCcam F182M imaging to best match NIRCspec. The kernel has axis ratio $q = 0.55$, but the NIRCspec/IFS PSF is the result of convolving this kernel with the NIRCcam PSF. The kernel position angle is 34° , meaning the NIRCspec/IFS PSF is elongated preferentially along the IFS slices.

slices) as

$$FWHM(\lambda) = (0.12 + 1.9 \cdot \lambda[\mu\text{m}] \cdot \exp(-24.4/\lambda[\mu\text{m}])) \text{ arcsec} \quad (3)$$

(dotted grey line in panel a) and along the minor axis (across slices) as

$$FWHM(\lambda) = (0.09 + 0.2 \cdot \lambda[\mu\text{m}] \cdot \exp(-12.5/\lambda[\mu\text{m}])) \text{ arcsec} \quad (4)$$

(dashed grey line in panel a).

Neither of the three methods adopted is ideal. For method I, we are using observations with a different number of dither positions than GS-10578, which may affect the image and PSF reconstruction; the limited number of dithers means we can only reconstruct the image with a scale of 0.05 arcsec/spaxel, which may limit the accuracy of the PSF modelling. For method II, the serendipitous star is close to the edge of the NIRSpec/IFS field of view, and may therefore suffer from edge effects. For method III, the starting NIRC*am* image has a different PSF than the NIRSpec/IFS image, therefore, there is no guarantee that a Gaussian (or two Gaussians) kernel can model the resulting image adequately. However, the fact that the three methods agree on the elongated shape of the PSF leads credence to our conclusion. Furthermore, the elongation of the PSF along the instrument slicers has already been reported by other authors (Parlanti et al., in prep., Perna et al., in prep.), was already expected from the instrument design and had already been noted during ground-based evaluations (Böker, T., priv. comm.).

When measuring the spin parameter λ_{R_c} , we apply an empirical correction to obtain the intrinsic value from the observed measurement [34]. We assume a PSF FWHM of 0.09 arcsec (at 2 μm); a larger FWHM value would increase the intrinsic λ_R and make our results more significant.

1.3 Redshift determination.

One would think that spectroscopy with spectral resolution of $R = 2,700$ ought to yield redshift uncertainties better than 10 km s⁻¹, i.e., a fraction of a pixel for well-sampled spectra (as is the case for NIRSpec). However, our data consists of two kind of spectral features, both of which are scarcely conducive of precise redshift determination. Nebular emission consists of broad lines and of multiple narrow lines. Even when a precise redshift can be determined, it is unclear which narrow lines can be used to trace the redshift of the galaxy. For the stellar features, the physical association with the systemic redshift is unambiguous, but all the absorption features belong to the Balmer series of hydrogen and are therefore subject to nebular-line infill. Line infill may consist of multiple components too.

To take into account the different ways the absorption lines can be filled we use a Monte Carlo approach. We consider the central spectrum as the unweighted sum of the spectra within the elliptical aperture of semi-major axis equal to $R_c/2$, axis ratio $q = 0.75$ and position angle 111.5°; spaxels partially inside the aperture are weighted according to the fractional overlap between the spaxel and the ellipse. We then create one thousand random-noise realisations of this spectrum by adding white noise from the uncertainty spectrum.

This procedure yields an ensemble of spectra that have 40 per cent lower S/N than the actual data, but crucially preserve any systematics compared to e.g., bootstrapping based on a best-fit model spectrum. We fit each random realisation with the same procedure used in § 1.5, but we also use a random starting guess for the redshift, chosen between $3.04 < z < 3.09$. The resulting redshift distribution is bimodal, with the strongest peak at $z = 3.06404$ and a secondary peak at $z = 3.06568$ (the two distributions contain 63 and 37 per cent of the total probability). We therefore adopt a systemic redshift $z_{\text{sys}} = 3.06404$. The random uncertainties (from a Gaussian

fit to the posterior distribution) are of order 0.0004, but this value is overestimated, because we added random noise to the already noisy spectrum. However, the systematic uncertainty (defined as the distance between the strongest and secondary peak) is much larger at 0.0016. The random and systematic redshift uncertainties correspond to velocity uncertainties of 31 km s^{-1} and 120 km s^{-1} , respectively. Our final redshift determination is $z_{\text{sys}} = 3.06404 \pm 0.0004(\text{rand.}) \pm 0.0016(\text{syst.})$.

Spectroscopy in band 1 (g140m and g140h gratings) may remove the systematic uncertainty entirely, by targeting the higher-order Balmer lines where the stellar absorption is much stronger than the nebular emission. However, even this region may present complex features (e.g., ISM absorption with high equivalent width in the Ca II doublet, which overlap with other stellar features (stellar Ca II and H ϵ).

1.4 Spectral energy distribution modelling and star-formation history

To study the physical properties of the stellar populations present in GS-10578, the prism/clear NIRSpec/IFS observations were analysed in a spaxel-by-spaxel basis (0.05 arcsec on a side) following a similar method to that described in [57]. Before comparing with models, the NIRSpec prism/clear data was PSF-matched using a Gaussian kernel to match the FWHM of the PSF at $4.5 \text{ }\mu\text{m}$, 0.16 arcsec FWHM (see Fig. 7a, dotted line) The spectra were also re-calibrated in flux (with correction factors ranging from 0.86 at $1 \text{ }\mu\text{m}$ to 1.29 at $2.0\text{--}2.5 \text{ }\mu\text{m}$) to match the integrated magnitude (in a 1.2 arcsec radius circular aperture) NIRCam wide- and medium-band data obtained by JADES [11, 12]. We considered a 5 per cent constant error added in quadrature to the formal observational values to account for the absolute flux calibration uncertainties.

The spectrum for each spaxel counting with more than 10 wavelengths with $S/N > 5$ was compared to a grid of stellar population models constructed with the [58] library, assuming a star formation history described by a delayed exponential characterised by a timescale τ (ranging from 1 Myr to 1 Gyr in 0.1 dex steps) and age t_0 (ranging from 1 Myr to the age of the Universe at the redshift of the galaxy, 2 Gyr). The stellar metallicity Z was left as a free parameter, allowing to take all the discrete values provided by the [58] library from 2 per cent solar to 2.5 times solar. Nebular (continuum and line) emission was taken into account as described in [59, 60]. The attenuation of the stellar and nebular emission was modelled with a [61] law, with A_V values ranging from 0 to 5 magnitudes in 0.1 mag steps. The (surviving, i.e., without including remnants and gas re-injected by winds and supernova explosions into the interstellar medium) stellar mass is obtained by scaling the (mass-normalised) stellar model to the spectrum (i.e., the stellar mass is not a directly fitted quantity).

The stellar population synthesis method includes a Monte Carlo algorithm to estimate uncertainties and degeneracies of the modelling (see [60, 62]), consisting in varying the data points according to their uncertainties, refitting the spectrum, and analysing the clusters of different solutions identified in the multi-dimensional parameter space defined by τ , t_0 , Z , and A_V .

Based on this method, we constructed the stellar mass and mass-weighted age maps presented in Fig. 2a–b. The mass-weighted age was calculated by integrating

the star formation history multiplied by the time from 0 to the age t_0 of the stellar population.

The integrated SFH and stellar mass evolution as well as the global spectral energy distribution, all presented in Fig. 2, were constructed by adding all the spaxels included in the stellar population synthesis analysis. To account for low surface brightness pixels that were not included in the modelling, we applied an aperture correction obtained by comparing the flux of the analysed spaxels compared to the integrated photometric aperture.

1.4.1 Modelling the panchromatic SED with CIGALE

The panchromatic SED of the target was built by considering the multi-wavelength UV-to-NIR photometry available in [63] as well as the NIRC*am* photometry released by the JADES and JEMS collaborations [11–13]. The MIR-to-FIR photometry was taken from [64]. The counterpart in the different catalogs was found by using a positional matching radius of 1 arcsec. The SED was then analyzed by using the galaxy SED-fitting tool CIGALE (Code Investigating GALaxy Emission; [65]). This code performs a multi-component fitting to separate the AGN contribution from the host galaxy emission. We used the following models to reproduce the different emission components: i) the stellar emission was modelled by adopting a delayed- τ (exponentially declining) SFH, the stellar population models of [58], a Chabrier initial mass function (IMF; [66]), and solar metallicity. Dust attenuation was taken into account through the modified version of the [67] curve available within CIGALE. ii) The emission from dust heated by star formation was reproduced using the model library by [68], where we assumed an AGN contribution equal to 0 in order to treat it separately. iii) The AGN emission component was reproduced by using the models presented by [69]. We run CIGALE by adopting the same input grid used by [70] and the CIGALE version v2018.0.2.

1.5 Stellar kinematics

We present the first spatially resolved stellar kinematics beyond redshift $z = 2.5$, and the first 2-d stellar kinematics beyond $z = 0.8$. For these measurements we use P_{PF}, which models simultaneously the stellar continuum and nebular lines with a non-linear χ^2 minimisation [54, 71, 72], all while taking into account the instrument line-spread function. The stellar continuum is modelled as a (non-negative) linear superposition of simple stellar population (SSP) spectra. As input, we use a subset of the SSPs library based on the MIST isochrones [73] and C3K model atmospheres [74]. The SSP templates span a logarithmically spaced grid of ages and metallicities, covering the ranges 10–2,500 Myr with 0.2 dex sampling and $[Z/H] = -2.00$ –0.25 dex with 0.25 dex sampling. The maximum age is set to 500 Myr older than the age of the Universe at the redshift of GS-10578, to avoid edge effects (changing this setting does not alter our conclusions). The nebular emission and absorption lines are modelled as multiple Gaussians. It is common practice to also use additive Legendre polynomials when fitting stellar kinematics [75], but we found that P_{PF} tended to fit a strongly negative and almost featureless polynomial, akin to an over-subtracted

background as bright as the target, which – given our flux calibration – is unphysical. We therefore used a 15th-order multiplicative Legendre polynomial to model residual flux-calibration issues. For the line-spread function, we use a uniform spectral resolution of $R = 2,700$, using the *nominal* resolution curve for g235h [47].

We find that our results depend critically on the wavelength range adopted. This is due to the already mentioned degeneracy between Balmer emission and absorption (S 1.3). For example, restricting the fit to the range where only H δ and H γ are present, we measure a σ_* that is 25 per cent lower (in this case the degree of the multiplicative polynomial is only 3). It is common practice to assess this uncertainty by repeating the fit and masking the Balmer lines [21], but in our case these lines are the only prominent stellar absorption features in the observed spectroscopic configuration. Therefore, as for the redshift, a conclusive test may require new observations at shorter wavelengths.

1.5.1 Aperture-integrated kinematics

We use two sets of aperture-integrated kinematics: inside an ellipse of semi-major axis equal to one R_e (for calculating the second moment of the line-of-sight velocity distribution of the stars, $\sigma_{*,e}$), and inside elliptical annuli (for use in the BPT diagram, Fig. 3). In both cases, we use emission lines coupled in four sets called ‘kinematic components’, which share the same line-of-sight velocity and intrinsic velocity dispersion (i.e., before convolution with the NIRSpect g235h line spread function). The first kinematic set consists of the Balmer series of hydrogen H δ –H α (using the intrinsic line ratios appropriate for Case B recombination, electron density $n_e = 100 \text{ cm}^{-3}$ and temperature $T_e = 10,000 \text{ K}$; note the relative line fluxes are then modified with a dust attenuation model), [N I] λ 5201, and the [O I] λ 6302,6366 doublet. The second component consists of the [O III] λ 4960,5008, [N II] λ 6550,6585 and [S II] λ 6718,6733 doublets. The third component consists of [O III] and [N II]. The fourth and last component is the resonant Na I D_1 and D_2 absorption features. The [O III], [O I] and [N II] doublets have line ratios fixed to the appropriate values from atomic physics; the [S II] doublet has line ratio constrained between 0.44 and 1.47 [76], and the D_2/D_1 ratio of Na I is constrained between 0.89 and 1.94 [77]. For nebular emission only, we use the [61] attenuation law.

From the elliptical aperture at $1 R_e$ we find $\sigma_{*,e} = 356 \pm 10 \text{ km s}^{-1}$. The uncertainties are likely dominated by systematics, so we consider the fiducial uncertainties to be 10 per cent. Using the virial theorem calibration of [30] and the light profile measurements from CANDELS [52] F160W imaging [22], we find a dynamical mass $M_{\text{dyn}} = k(n)k(q)\sigma_{*,e}^2 R_e / G = (2.0 \pm 0.1) \times 10^{11} M_\odot$, dominated by the scatter in the calibration, which are of order 25 per cent. For a single-burst stellar population of age 1 Gyr, the surviving stellar mass fraction is 0.7 (assuming a Chabrier initial mass function and solar metallicity). Down-scaling the stellar mass formed by this factor, we obtain a dynamical-to-stellar mass ratio of 70 per cent.

We also use the $1 R_e$ apertures to measure the Balmer EW indices H δ_A and H γ_A , using the Lick definition [78]. For H δ_A , the Lick bands lie partially outside the wavelength range of the g235h/f170lp datacube. We therefore measure the H δ absorption strength using the best-fit model. The resulting values are H $\delta_A = 6.63 \pm 0.01$ and

$8.06 \pm 0.08 \text{ \AA}$ (rest frame), where for the second value we subtracted the nebular emission. The uncertainties are from bootstrapping the uncertainties on the data. Clearly, the true stellar EW must be higher than the non-subtracted measurement, which lies itself well into the range that defines PSB galaxies ($H\delta_A > 4\text{--}5 \text{ \AA}$, e.g., [79]). For $H\gamma_A$, we can measure the index from the data, and find respectively $H\gamma_A = 4.07 \pm 0.01$ and $6.83 \pm 0.09 \text{ \AA}$ for the unsubtracted and subtracted spectra. Both values are again in the PSB regime.

1.5.2 Spatially resolved stellar kinematics

Measuring spatially resolved stellar kinematics with `PPXF` typically requires $S/N \gtrsim 10\text{--}15 \text{ \AA}^{-1}$, unless specific constraints are applied [75]. Our data has a continuum S/N as low as $3\text{--}5 \text{ \AA}^{-1}$, therefore we need to adopt a careful approach. We measure spatially resolved stellar kinematics with two different setups: Voronoi-binned data (Method I) and spaxel-by-spaxel measurements (Method II). Briefly, Voronoi bins have the advantage of higher S/N [80], but for data with low spatial resolution they risk averaging over regions with different stellar populations and kinematics [75]; spaxel-by-spaxel fitting overcomes the low- S/N limitations by restricting the set of input templates [75, 81]. The results in the article are based on Method I. The other method is described only briefly, to show that our findings do not depend on the procedure adopted.

Method I – Voronoi-binned data. We measure the S/N per spaxel with a preliminary fit to each spaxel independently, using the the best-fit template from the fit to the aperture spectrum as the only input template (1.5.1). The S/N is then measured from the standard deviation of the residuals between the spaxel best-fit model and the data. Having determined the S/N empirically, we proceed to create the Voronoi bins using `VORBIN` [80]. We select a target $S/N = 12 \text{ \AA}^{-1}$. The resulting bins are outlined in Fig. 5a and are colour-coded by their empirical S/N , estimated from the residuals of the `PPXF` fit (see below); we note that in the outer bins ($1 < R < 2 R_c$) the empirical S/N is lower than the target S/N . This outcome is in fact expected from correlated noise, which becomes more relevant as the average size of the Voronoi bins increases outward from the galaxy centre.

To fit each spectrum, we use the same procedure as for the integrated spectrum, but the choice of SSP spectra is restricted only to the spectra that had non-zero weight in the linear combination forming the best-fit aperture spectrum.

Moreover, the selection of Gaussian templates representing nebular emission and absorption is also simplified compared to what we used for the aperture spectrum, reflecting the simpler kinematics of the spatially resolved spectra. The first kinematic component consisting of the $H\delta\text{--}H\alpha$ series, the $[O\text{ III}]\lambda\lambda 4960, 5008$ doublet, $[N\text{ I}]\lambda 5201$ and the three doublets $[O\text{ I}]\lambda\lambda 6302, 6366$, $[N\text{ II}]\lambda\lambda 6550, 6585$ and $[S\text{ II}]\lambda\lambda 6718, 6733$. The second kinematic component consists of $[O\text{ III}]\lambda\lambda 4960, 5008$ and $[N\text{ II}]\lambda\lambda 6550, 6585$, and the third kinematic component consists of Na I absorption. All doublets are fixed or constrained, as described for the aperture kinematics. Example fits of Voronoi bins are shown in Fig. 5e and f.

Method II – Spaxel-by-spaxel data. To measure spaxel-by-spaxel kinematics, we use a threshold $S/N > 3 \text{ pixel}^{-1}$. In general, such a low value is considered sub-optimal, but if the templates are carefully pre-selected, it is still possible to obtain accurate measurements [75]. To optimise the templates selection, we first create 11 annular-binned spectra between 0 and $2.5 R_e$, spaced by 0.025 arcsec and with the same shape and position angle as the observed stellar continuum. We then de-rotate the spectrum in each spaxel according to the line-of-sight velocity measured in the relevant Voronoi bins; this avoids the spectral broadening due to rotation. The resulting bin spectra are fit with the same procedure as for the Voronoi bins. From these fits we take the weights of the SSP templates and the measured σ_* . We then proceed to fit the individual spaxels. Given a spaxel, we identify the annular bins that the spaxel intersects and then also consider two more bins (if they exist): the annulus adjacent to the innermost selected annulus and the annulus adjacent to the outermost selected annulus. The template selection is simply the union of all non-zero templates from the best-fit annular spectra (typically 7–9 templates are selected). The velocity dispersion is the average of the annular σ_* values, weighted by the fractional overlap of the spaxel with the annuli. We fit the spaxel spectrum using this restricted template selection and with σ_* fixed to the average σ_* . If the resulting fit has $S/N < 5$, the fit is concluded and we proceed to another spaxel. If the resulting fit has $S/N > 5$, we repeat the fit leaving σ_* free between ± 30 per cent from the input σ_* . The uncertainties are measured again using bootstrapping. The resulting maps are shown in Fig. 9, where we compare them with the Voronoi-binned maps. The resulting velocity values are quantitatively different, but the results are qualitatively the same. σ_* shows higher values in the central regions, likely due to a combination of lower average S/N and smaller template set compared to the Voronoi bins. Using this method, we measure a spin parameter $\lambda_{R_c} = 0.40$, which rises to 0.60 after the PSF correction; this latter value is consistent with the measurement from Method I.

1.6 Emission-line measurements

To measure the line-of-sight velocity and velocity width of the nebular emission lines, we used QUBESPEC algorithm. We modelled simultaneously [O III] $\lambda\lambda 4960, 5008$, H α and [N II] $\lambda\lambda 6550, 6585$. Each emission line was modelled with a single or a double Gaussian profile, with the redshift and FWHM of each Gaussian component being the same between the individual emission lines. We fixed the flux ratio of the [O III] and [N II] doublets as described in S 1.5. We estimate the posterior probability distribution of both the single- and double-Gaussian models with the Markov-Chain Monte-Carlo algorithm EMCEE [55]. We select the best model (either one or two Gaussians per emission line) based on the Bayesian Information Criterion [BIC; 82]. For each spaxel, we took a median spectrum of within the PSF (± 2 spaxel) to increase the S/N of each fitted spectrum, while maintaining the diffraction-limited spatial resolution.

For each fitted spaxel, we calculated the v_{10} , v_{50} , v_{90} and w_{80} as velocities of 10th, 50th and 90th velocity percentiles of the emission line and the velocity width of the line 80 per cent of the flux ($v_{90}-v_{10}$). The systemic velocity of the galaxy (v_0) was set

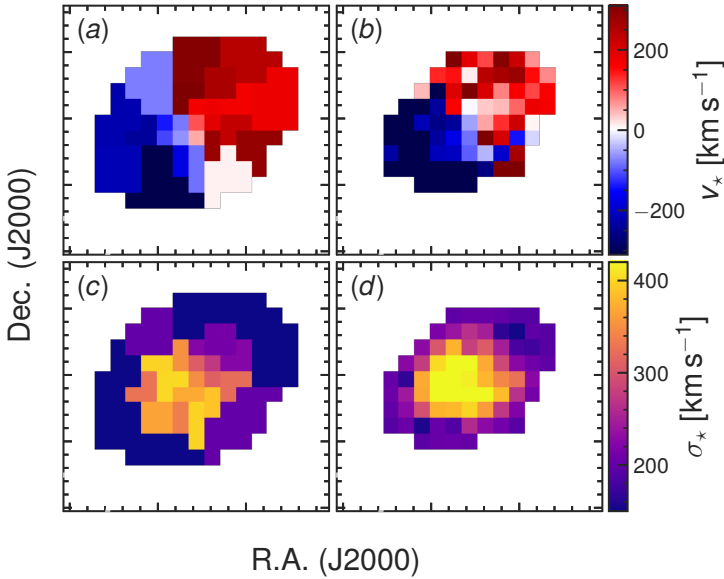


Fig. 9: Comparison of the stellar kinematics between the fiducial method (based on Voronoi bins, Method I; panels **a** and **c**) and the alternative method (based on individual spaxel with constrained templates, Method II; panels **b** and **d**). The two measurements show good agreement, but the spaxel-by-spaxel fits tend to find higher σ_* in the centre, possibly due to lower S/N and smaller set of input templates for the fit.

to the systemic velocity of the stellar component (S 1.3). Despite each of the Gaussian components fitted having the same redshift and FWHM, the final kinematics can be different due to different flux ratios of the Gaussian components in each emission line. The resulting flux and kinematic maps are presented in Fig. 4.

1.7 Outflow measurements

To estimate the outflow rate of the ionised gas, we used the [O III] emission line. Because H β is only seen in absorption, we calculated the mass of the outflowing ionised gas from the [O III] line as follows (see e.g. [83, 84])

$$M_{\text{out}}^{[\text{O III}]} = 8 \cdot 10^7 \left(\frac{1}{10^{[\text{O}/\text{H}] - [\text{O}/\text{H}]_{\odot}}} \right) \left(\frac{L_{[\text{O III}]}}{10^{44} \text{ erg s}^{-1}} \right) \left(\frac{n_e}{500 \text{ cm}^{-3}} \right)^{-1} M_{\odot} \quad (5)$$

where $L_{[\text{O III}]}$ is the line luminosity, n_e is the mean electron density, and where we assumed that the electron temperature is 10,000 K, all the oxygen is ionised to O²⁺, and the metallicity [O/H] of the outflowing material is equal to the solar value [O/H]_⊙. We further assume a uniformly filled biconical outflow, and use the equation from

[85] as

$$\dot{M}_{\text{out}} = 3 \cdot v_{\text{out}} \frac{M_{\text{out}}}{R_{\text{out}}} \quad (6)$$

where v_{out} is the velocity of the outflows (defined as $v_{\text{out}} = v_{10} = 1,200 \text{ km s}^{-1}$), M_{out} is the outflowing mass and R_{out} is the radius of the outflow. The latter was estimated in the w_{80} map as the radius of the region where $w_{80} > 600 \text{ km s}^{-1}$ [84, 86]. This value corresponded to a radius $R_{\text{out}} = 3.57 \text{ kpc}$. The largest source of uncertainty in this calculation is n_e , which can range from 500 to 10^4 cm^{-3} (e.g., [87, 88]). Therefore, we estimated the outflow rate for the range of density values, resulting in an outflow rate in ionised gas of $0.14\text{--}2.9 \text{ M}_{\odot} \text{ yr}^{-1}$. This range is shown as the range of the cyan errorbars in Fig. 2c.

For the neutral gas outflows, we use the methods of [89], based on the Na I absorption. These authors extend the methods of [90] to spatially resolved spectroscopy. We assume a thin-shell, conical geometry orthogonal to the galaxy disc; [91] remark that assuming a conical geometry with uniform density changes the outflow rate by a factor of 3. Our disc inclination is 66° , from the axis ratio of the best-fit Sérsic model [22]. The outflow rate in the k^{th} spaxel is

$$\dot{M}_{\text{out},k}^{\text{NaI}} = 11.5 \left(\frac{R_{\text{out}}}{10 \text{ kpc}} \right) \left(C_f \frac{\Omega_k}{0.4} \right) \left(\frac{N_k}{10^{21} \text{ cm}^{-2}} \right) \left(\frac{v_{\text{out},k}}{200 \text{ km s}^{-1}} \right) \text{ M}_{\odot} \text{ yr}^{-1} \quad (7)$$

where R_{out} is the extent of the outflow, Ω_k is the subtended solid angle, $C_f = 0.37$ is the cloud covering fraction (estimated from [90]), N_k is the gas column density, and $v_{\text{out},k}$ is the outflow physical velocity. The extent of the outflow is $R_{\text{out}} = 2.7 \text{ kpc}$, estimated as the distance between the centre of the galaxy and the outermost detected Na I absorption, corrected for inclination. As noted by e.g., [89], this size measurement relies on the presence of a sufficiently bright background illumination to detect foreground Na I absorption, therefore we can consider R_{out} a lower limit to the true extent of the outflow. The solid angle subtended by each spaxel is calculated from the spherical shell geometry. N_k is estimated from the equivalent width of Na I using Eq. 1 from [89]; our equivalent-width measurements are corrected for the contribution due to the stellar atmospheric absorption. The outflow velocity is taken from the ppxf fits, and is the (absolute value) of the centroid Gaussian-line velocity, corrected for the outflow inclination by $\cos i$.

From this formula, summing over all spaxels where we detect blueshifted Na I absorption, we obtain $\dot{M}_{\text{out}}^{\text{NaI}} = 100 \text{ M}_{\odot} \text{ yr}^{-1}$.

To estimate the escape velocity v_{esc} , we need the gravitational potential of the galaxy, including its dark matter halo. Using the relation between stellar mass and halo mass to infer the mass of the dark matter halo is impractical. This is because – for the stellar mass of GS-10578 – the slope of the relation is unfavourable for a precise inference. We adopt the alternative method of assuming the gravitational potential of the galaxy is an isothermal sphere, truncated at a radius r_{max} [56, 92, 93]. Using Eq 4 from [56] with $r_{\text{max}} = 100 \text{ kpc}$, we obtain an escape

velocity $v_{\text{esc}} = 1,200 \pm 200 \text{ km s}^{-1}$. The uncertainties were estimated with a simple Monte-Carlo analysis, where we have randomly drawn the various observables that go into the equation of v_{esc} as follows. Aperture velocity dispersion $\sigma_{\star,e}$ is drawn from the normal distribution $\mathcal{N}(\mu, \sigma)$ with mean $\mu = 356$ and standard deviation $\sigma = 36 \text{ km s}^{-1}$ (ten per cent); R_e is drawn from $\mathcal{N}(0.14, 0.02)$ (units of kpc); Sérsic index n is from the truncated normal distribution $\mathcal{T}(\mu, \sigma; \mu_0, \mu_1)$ with mean $\mu = 1.96$, $\sigma = 0.4$ (twenty per cent), and truncated between $\mu_0 = 1$ and $\mu_1 = 4$; the r_{out} is from $\mathcal{T}(4.5, 1, 2.5, 6)$ (units of spaxels); the galaxy intrinsic axis ratio q_0 is from $\mathcal{T}(0.2, 0.1, 0.1, 0.5)$, and the projected axis ratio q is from $\mathcal{T}(0.44, 0.1, 0.3, 0.5)$, subject to $q \geq q_0$; q and q_0 are used to infer the inclination i .

Most of the uncertainty on v_{esc} is due to the outflow radius r_{out} (60 per cent), followed by $\sigma_{\star,e}$ (30 per cent) and R_e (10 per cent); the other three variables account for a few per cent each. Comparing our v_{esc} to the map of de-projected Na I velocities (Fig. 5c), we find an average ratio $|v_{\text{NaI}}|/v_{\text{esc}} = 0.8 \pm 0.2$. Given the uncertainties on the outflow geometry and escape velocity, we can conclude that at least part of the neutral-gas outflows are able to escape the galaxy gravitational potential. At the very least, the gas will be temporarily removed from the star-forming region.

Comparing the ionised and neutral outflow phases, we conclude that the ionised-gas outflow rate is negligible, being up to two orders of magnitude lower than the neutral-gas outflow rate. The mass loading factor of the neutral outflow is orders higher than the recent SFR, therefore this outflow is sufficient to *stop* star formation. Similar events in the recent past of GS-10578 may have caused the galaxy to become quiescent (see SFH in 2b).

Data availability The data that support the findings of this study are publicly available from the [Mikulski Archive for Space Telescopes](#).

Code availability This work made extensive use of the freely available [Debian GNU/Linux](#) operative system. We used the [Python](#) programming language [94], maintained and distributed by the Python Software Foundation. We further acknowledge direct use of [astropy](#) [95], [dynesty](#) [96], [fsps](#) [97, 98], [matplotlib](#) [99], [numpy](#) [100], [prospector](#) [101] [python-fsps](#) [102], and [scipy](#) [103].

Acknowledgements

FDE, TJL, RM and JS and acknowledge support by the Science and Technology Facilities Council (STFC), by the ERC Advanced Grant 695671 “QUENCH”, and by the UKRI Frontier Research grant RISEandFALL; RM is further supported by a research professorship from the Royal Society. PGP-G acknowledges support grants PGC2018-093499-B-I00 and PID2022-139567NB-I00 funded by Spanish Ministerio de Ciencia e Innovación MCIN/AEI/10.13039/501100011033, FEDER, UE. SA, BRP, and MP acknowledge support from the research project PID2021-127718NB-I00 of the Spanish Ministry of Science and Innovation/State Agency of Research (MICIN/AEI). MP is further supported by the Programa Atracción de Talento de la Comunidad de Madrid via grant 2018-T2/TIC-11715. HÜ gratefully acknowledges support by the Isaac Newton Trust and by the Kavli Foundation through

a Newton-Kavli Junior Fellowship. AJB, JC and GCJ acknowledge funding from the “First-Galaxies” Advanced Grant from the European Research Council (ERC) under the European Union’s Horizon 2020 research and innovation programme (Grant agreement No. 789056). SC, EP and GV acknowledge support by European Union’s HE ERC Starting Grant No. 101040227 - WINGS. GC acknowledges the support of the INAF Large Grant 2022 “The metal circle: a new sharp view of the baryon cycle up to Cosmic Dawn with the latest generation IFU facilities” IL acknowledges support from PID2022-140483NB-C22 funded by AEI 10.13039/501100011033 and BDC 20221289 funded by MCIN by the Recovery, Transformation and Resilience Plan from the Spanish State, and by NextGenerationEU from the European Union through the Recovery and Resilience Facility. BER acknowledges support from the NIRCAM Science Team contract to the University of Arizona, NAS5-02015. The authors acknowledge use of the lux supercomputer at UC Santa Cruz, funded by NSF MRI grant AST 1828315.

References

- [1] Madau, P., Dickinson, M.: Cosmic Star-Formation History. *ARA&A* **52**, 415–486 (2014) <https://arxiv.org/abs/1403.0007> [astro-ph.CO]. <https://doi.org/10.1146/annurev-astro-081811-125615>
- [2] Thomas, D., Maraston, C., Schawinski, K., Sarzi, M., Silk, J.: Environment and self-regulation in galaxy formation. *MNRAS* **404**, 1775–1789 (2010) <https://arxiv.org/abs/0912.0259>. <https://doi.org/10.1111/j.1365-2966.2010.16427.x>
- [3] McDermid, R.M., Alatalo, K., Blitz, L., Bournaud, F., Bureau, M., Cappellari, M., Crocker, A.F., Davies, R.L., Davis, T.A., de Zeeuw, P.T., Duc, P.-A., Emsellem, E., Khochfar, S., Krajnović, D., Kuntschner, H., Morganti, R., Naab, T., Oosterloo, T., Sarzi, M., Scott, N., Serra, P., Weijmans, A.-M., Young, L.M.: The ATLAS^{3D} Project - XXX. Star formation histories and stellar population scaling relations of early-type galaxies. *MNRAS* **448**, 3484–3513 (2015) <https://arxiv.org/abs/1501.03723>. <https://doi.org/10.1093/mnras/stv105>
- [4] Whitaker, K.E., Williams, C.C., Mowla, L., Spilker, J.S., Toft, S., Narayanan, D., Pope, A., Magdis, G.E., van Dokkum, P.G., Akhshik, M., Bezanson, R., Brammer, G.B., Leja, J., Man, A., Nelson, E.J., Richard, J., Pacifici, C., Sharon, K., Valentino, F.: Quenching of star formation from a lack of inflowing gas to galaxies. *Nature* **597**(7877), 485–488 (2021) <https://arxiv.org/abs/2109.10384> [astro-ph.GA]. <https://doi.org/10.1038/s41586-021-03806-7>
- [5] Williams, C.C., Spilker, J.S., Whitaker, K.E., Davé, R., Woodrum, C., Brammer, G., Bezanson, R., Narayanan, D., Weiner, B.: ALMA Measures Rapidly Depleted Molecular Gas Reservoirs in Massive Quiescent Galaxies at $z \sim 1.5$. *ApJ* **908**(1), 54 (2021) <https://arxiv.org/abs/2012.01433> [astro-ph.GA]. <https://doi.org/10.3847/1538-4357/abcbf6>

- [6] Man, A., Belli, S.: Star formation quenching in massive galaxies. *Nature Astronomy* **2**, 695–697 (2018) <https://arxiv.org/abs/1809.00722> [astro-ph.GA]. <https://doi.org/10.1038/s41550-018-0558-1>
- [7] Somerville, R.S., Davé, R.: Physical Models of Galaxy Formation in a Cosmological Framework. *ARA&A* **53**, 51–113 (2015) <https://arxiv.org/abs/1412.2712> [astro-ph.GA]. <https://doi.org/10.1146/annurev-astro-082812-140951>
- [8] Barro, G., Faber, S.M., Pérez-González, P.G., Koo, D.C., Williams, C.C., Kocevski, D.D., Trump, J.R., Mozena, M., McGrath, E., van der Wel, A., Wuyts, S., Bell, E.F., Croton, D.J., Ceverino, D., Dekel, A., Ashby, M.L.N., Cheung, E., Ferguson, H.C., Fontana, A., Fang, J., Giavalisco, M., Grogin, N.A., Guo, Y., Hathi, N.P., Hopkins, P.F., Huang, K.-H., Koekemoer, A.M., Kartaltepe, J.S., Lee, K.-S., Newman, J.A., Porter, L.A., Primack, J.R., Ryan, R.E., Rosario, D., Somerville, R.S., Salvato, M., Hsu, L.-T.: CANDELS: The Progenitors of Compact Quiescent Galaxies at $z \sim 2$. *ApJ* **765**(2), 104 (2013) <https://arxiv.org/abs/1206.5000> [astro-ph.CO]. <https://doi.org/10.1088/0004-637X/765/2/104>
- [9] Damjanov, I., McCarthy, P.J., Abraham, R.G., Glazebrook, K., Yan, H., Mentuch, E., Le Borgne, D., Savaglio, S., Crampton, D., Murowinski, R., Juneau, S., Carlberg, R.G., Jørgensen, I., Roth, K., Chen, H.-W., Marzke, R.O.: Red Nuggets at $z \sim 1.5$: Compact Passive Galaxies and the Formation of the Kormendy Relation. *ApJ* **695**(1), 101–115 (2009) <https://arxiv.org/abs/0807.1744> [astro-ph]. <https://doi.org/10.1088/0004-637X/695/1/101>
- [10] Dekel, A., Burkert, A.: Wet disc contraction to galactic blue nuggets and quenching to red nuggets. *MNRAS* **438**(2), 1870–1879 (2014) <https://arxiv.org/abs/1310.1074> [astro-ph.CO]. <https://doi.org/10.1093/mnras/stt2331>
- [11] Eisenstein, D.J., Willott, C., Alberts, S., Arribas, S., Bonaventura, N., Bunker, A.J., Cameron, A.J., Carniani, S., Charlot, S., Curtis-Lake, E., D’Eugenio, F., Endsley, R., Ferruit, P., Giardino, G., Hainline, K., Hausen, R., Jakobsen, P., Johnson, B.D., Maiolino, R., Rieke, M., Rieke, G., Rix, H.-W., Robertson, B., Stark, D.P., Tacchella, S., Williams, C.C., Willmer, C.N.A., Baker, W.M., Baum, S., Bhatwadekar, R., Boyett, K., Chen, Z., Chevallard, J., Circosta, C., Curti, M., Danhaive, A.L., DeCoursey, C., de Graaff, A., Dressler, A., Egami, E., Helton, J.M., Hviding, R.E., Ji, Z., Jones, G.C., Kumari, N., Lützgendorf, N., Laseter, I., Looser, T.J., Lyu, J., Maseda, M.V., Nelson, E., Parlanti, E., Perna, M., Puskás, D., Rawle, T., Rodríguez Del Pino, B., Sandles, L., Saxena, A., Scholtz, J., Sharpe, K., Shivaiei, I., Silcock, M.S., Simmonds, C., Skarbinski, M., Smit, R., Stone, M., Suess, K.A., Sun, F., Tang, M., Topping, M.W., Übler, H., Villanueva, N.C., Wallace, I.E.B., Whitler, L., Witstok, J., Woodrum, C.: Overview of the JWST Advanced Deep Extragalactic Survey (JADES). *arXiv e-prints*, 2306–02465 (2023) <https://arxiv.org/abs/2306.02465> [astro-ph.GA]. <https://doi.org/10.48550/arXiv.2306.02465>

- [12] Rieke, M., Robertson, B., Tacchella, S., Hainline, K., Johnson, B., Hausen, R., Ji, Z., Willmer, N.A.C., the JADES Collaboration: JADES Initial Data Release for the Hubble Ultra Deep Field: Revealing the Faint Infrared Sky with Deep JWST NIRC*am* Imaging. arXiv e-prints, 2306–02466 (2023) <https://arxiv.org/abs/2306.02466> [astro-ph.GA]. <https://doi.org/10.48550/arXiv.2306.02466>
- [13] Williams, C.C., Tacchella, S., Maseda, M.V., Robertson, B.E., Johnson, B.D., Willott, C.J., Eisenstein, D.J., Willmer, C.N.A., Ji, Z., Hainline, K.N., Helton, J.M., Alberts, S., Baum, S., Bhatawdekar, R., Boyett, K., Bunker, A.J., Carniani, S., Charlot, S., Chevillard, J., Curtis-Lake, E., de Graaf, A., Egami, E., Franx, M., Kumari, N., Maiolino, R., Nelson, E.J., Rieke, M.J., Sandles, L., Shiva*ei*, I., Simmonds, C., Smit, R., Suess, K.A., Sun, F., Ubler, H., Witstok, J.: JEMS: A deep medium-band imaging survey in the Hubble Ultra-Deep Field with JWST NIRC*am* & NIRISS. arXiv e-prints, 2301–09780 (2023) <https://arxiv.org/abs/2301.09780> [astro-ph.GA]. <https://doi.org/10.48550/arXiv.2301.09780>
- [14] Suess, K.A., Williams, C.C., Robertson, B., Ji, Z., Johnson, B.D., Nelson, E., Alberts, S., Hainline, K., DEugenio, F., Ubler, H., Rieke, M., Rieke, G., Bunker, A.J., Carniani, S., Charlot, S., Eisenstein, D.J., Maiolino, R., Stark, D.P., Tacchella, S., Willott, C.: Minor merger growth in action: JWST detects faint blue companions around massive quiescent galaxies at $0.5 < z < 3$. arXiv e-prints, 2307–14209 (2023) <https://arxiv.org/abs/2307.14209> [astro-ph.GA]. <https://doi.org/10.48550/arXiv.2307.14209>
- [15] Popesso, P., Concas, A., Cresci, G., Belli, S., Rodighiero, G., Inami, H., Dickinson, M., Ilbert, O., Pannella, M., Elbaz, D.: The main sequence of star-forming galaxies across cosmic times. MNRAS **519**(1), 1526–1544 (2023) <https://arxiv.org/abs/2203.10487> [astro-ph.GA]. <https://doi.org/10.1093/mnras/stac3214>
- [16] Pacifici, C., Kassin, S.A., Weiner, B.J., Holden, B., Gardner, J.P., Faber, S.M., Ferguson, H.C., Koo, D.C., Primack, J.R., Bell, E.F., Dekel, A., Gawiser, E., Giavalisco, M., Rafelski, M., Simons, R.C., Barro, G., Croton, D.J., Davé, R., Fontana, A., Grogin, N.A., Koekemoer, A.M., Lee, S.-K., Salmon, B., Somerville, R., Behroozi, P.: The Evolution of Star Formation Histories of Quiescent Galaxies. ApJ **832**(1), 79 (2016) <https://arxiv.org/abs/1609.03572> [astro-ph.GA]. <https://doi.org/10.3847/0004-637X/832/1/79>
- [17] Williams, R.J., Quadri, R.F., Franx, M., van Dokkum, P., Labbé, I.: Detection of Quiescent Galaxies in a Bicolor Sequence from $Z = 0-2$. ApJ **691**(2), 1879–1895 (2009) <https://arxiv.org/abs/0806.0625> [astro-ph]. <https://doi.org/10.1088/0004-637X/691/2/1879>
- [18] Kauffmann, G., Heckman, T.M., Tremonti, C., Brinchmann, J., Charlot, S., White, S.D.M., Ridgway, S.E., Brinkmann, J., Fukugita, M., Hall, P.B.,

- Ivezić, Ž., Richards, G.T., Schneider, D.P.: The host galaxies of active galactic nuclei. *MNRAS* **346**, 1055–1077 (2003) <https://arxiv.org/abs/astro-ph/0304239>. <https://doi.org/10.1111/j.1365-2966.2003.07154.x>
- [19] Curti, M., Maiolino, R., Cirasuolo, M., Mannucci, F., Williams, R.J., Auger, M., Mercurio, A., Hayden-Pawson, C., Cresci, G., Marconi, A., Belfiore, F., Cappellari, M., Cicone, C., Cullen, F., Meneghetti, M., Ota, K., Peng, Y., Pettini, M., Swinbank, M., Troncoso, P.: The KLEVER Survey: spatially resolved metallicity maps and gradients in a sample of $1.2 < z < 2.5$ lensed galaxies. *MNRAS* **492**(1), 821–842 (2020) <https://arxiv.org/abs/1910.13451> [astro-ph.GA]. <https://doi.org/10.1093/mnras/stz3379>
- [20] Newman, A.B., Belli, S., Ellis, R.S., Patel, S.G.: Resolving Quiescent Galaxies at $z \gtrsim 2$. I. Search for Gravitationally Lensed Sources and Characterization of Their Structure, Stellar Populations, and Line Emission. *ApJ* **862**(2), 125 (2018) <https://arxiv.org/abs/1806.06814> [astro-ph.GA]. <https://doi.org/10.3847/1538-4357/aacd4d>
- [21] Newman, A.B., Belli, S., Ellis, R.S., Patel, S.G.: Resolving Quiescent Galaxies at $z \gtrsim 2$. II. Direct Measures of Rotational Support. *ApJ* **862**(2), 126 (2018) <https://arxiv.org/abs/1806.06815> [astro-ph.GA]. <https://doi.org/10.3847/1538-4357/aacd4f>
- [22] van der Wel, A., Franx, M., van Dokkum, P.G., Skelton, R.E., Momcheva, I.G., Whitaker, K.E., Brammer, G.B., Bell, E.F., Rix, H.-W., Wuyts, S., Ferguson, H.C., Holden, B.P., Barro, G., Koekemoer, A.M., Chang, Y.-Y., McGrath, E.J., Häussler, B., Dekel, A., Behroozi, P., Fumagalli, M., Leja, J., Lundgren, B.F., Maseda, M.V., Nelson, E.J., Wake, D.A., Patel, S.G., Labbé, I., Faber, S.M., Grogin, N.A., Kocevski, D.D.: 3D-HST+CANDELS: The Evolution of the Galaxy Size-Mass Distribution since $z = 3$. *ApJ* **788**(1), 28 (2014) <https://arxiv.org/abs/1404.2844> [astro-ph.GA]. <https://doi.org/10.1088/0004-637X/788/1/28>
- [23] Luo, B., Brandt, W.N., Xue, Y.Q., Lehmer, B., Alexander, D.M., Bauer, F.E., Vito, F., Yang, G., Basu-Zych, A.R., Comastri, A., Gilli, R., Gu, Q.-S., Hornschemeier, A.E., Koekemoer, A., Liu, T., Mainieri, V., Paolillo, M., Ranalli, P., Rosati, P., Schneider, D.P., Shemmer, O., Smail, I., Sun, M., Tozzi, P., Vignali, C., Wang, J.-X.: The Chandra Deep Field-South Survey: 7 Ms Source Catalogs. *ApJS* **228**(1), 2 (2017) <https://arxiv.org/abs/1611.03501> [astro-ph.GA]. <https://doi.org/10.3847/1538-4365/228/1/2>
- [24] Circosta, C., Vignali, C., Gilli, R., Feltre, A., Vito, F., Calura, F., Mainieri, V., Massardi, M., Norman, C.: X-ray emission of $z > 2.5$ active galactic nuclei can be obscured by their host galaxies. *A&A* **623**, 172 (2019) <https://arxiv.org/abs/1901.07108> [astro-ph.GA]. <https://doi.org/10.1051/0004-6361/201834426>
- [25] Cresci, G., Maiolino, R.: Observing positive and negative AGN feedback.

- Nature Astronomy **2**, 179–180 (2018) <https://arxiv.org/abs/1802.10305> [astro-ph.GA]. <https://doi.org/10.1038/s41550-018-0404-5>
- [26] Harrison, C.M., Costa, T., Tadhunter, C.N., Flütsch, A., Kakkad, D., Perna, M., Vietri, G.: AGN outflows and feedback twenty years on. Nature Astronomy **2**, 198–205 (2018) <https://arxiv.org/abs/1802.10306> [astro-ph.GA]. <https://doi.org/10.1038/s41550-018-0403-6>
- [27] Förster Schreiber, N.M., Übler, H., Davies, R.L., Genzel, R., Wisnioski, E., Belli, S., Shimizu, T., Lutz, D., Fossati, M., Herrera-Camus, R., Mendel, J.T., Tacconi, L.J., Wilman, D., Beifiori, A., Brammer, G.B., Burkert, A., Carollo, C.M., Davies, R.I., Eisenhauer, F., Fabricius, M., Lilly, S.J., Momcheva, I., Naab, T., Nelson, E.J., Price, S.H., Renzini, A., Saglia, R., Sternberg, A., van Dokkum, P., Wuyts, S.: The KMOS^{3D} Survey: Demographics and Properties of Galactic Outflows at $z = 0.6$ – 2.7 . ApJ **875**(1), 21 (2019) <https://arxiv.org/abs/1807.04738> [astro-ph.GA]. <https://doi.org/10.3847/1538-4357/ab0ca2>
- [28] Nelson, D., Pillepich, A., Springel, V., Pakmor, R., Weinberger, R., Genel, S., Torrey, P., Vogelsberger, M., Marinacci, F., Hernquist, L.: First results from the TNG50 simulation: galactic outflows driven by supernovae and black hole feedback. MNRAS **490**(3), 3234–3261 (2019) <https://arxiv.org/abs/1902.05554> [astro-ph.GA]. <https://doi.org/10.1093/mnras/stz2306>
- [29] Concas, A., Maiolino, R., Curti, M., Hayden-Pawson, C., Cirasuolo, M., Jones, G.C., Mercurio, A., Belfiore, F., Cresci, G., Cullen, F., Mannucci, F., Marconi, A., Cappellari, M., Cicone, C., Peng, Y., Troncoso, P.: Being KLEVER at cosmic noon: Ionized gas outflows are inconspicuous in low-mass star-forming galaxies but prominent in massive AGN hosts. MNRAS **513**(2), 2535–2562 (2022) <https://arxiv.org/abs/2203.11958> [astro-ph.GA]. <https://doi.org/10.1093/mnras/stac1026>
- [30] van der Wel, A., Houdt, J.v., Bezanson, R., Franx, M., D’Eugenio, F., Straatman, C., Bell, E.F., Muzzin, A., Sobral, D., Maseda, M.V., de Graaff, A., Holden, B.P.: The Mass Scale of High-redshift Galaxies: Virial Mass Estimates Calibrated with Stellar Dynamical Models from LEGA-C. ApJ **936**(1), 9 (2022) <https://arxiv.org/abs/2208.12605> [astro-ph.GA]. <https://doi.org/10.3847/1538-4357/ac83c5>
- [31] Bois, M., Bournaud, F., Emsellem, E., Alatalo, K., Blitz, L., Bureau, M., Cappellari, M., Davies, R.L., Davis, T.A., de Zeeuw, P.T., Duc, P.-A., Khochfar, S., Krajnović, D., Kuntschner, H., Lablanche, P.-Y., McDermid, R.M., Morganti, R., Naab, T., Oosterloo, T., Sarzi, M., Scott, N., Serra, P., Weijmans, A., Young, L.M.: Formation of slowly rotating early-type galaxies via major mergers: a resolution study. MNRAS **406**(4), 2405–2420 (2010) <https://arxiv.org/abs/1004.4003> [astro-ph.CO]. <https://doi.org/10.1111/j.1365-2966.2010.16885.x>

- [32] Emsellem, E., Cappellari, M., Krajnović, D., van de Ven, G., Bacon, R., Bureau, M., Davies, R.L., de Zeeuw, P.T., Falcón-Barroso, J., Kuntschner, H., McDermid, R., Peletier, R.F., Sarzi, M.: The SAURON project - IX. A kinematic classification for early-type galaxies. *MNRAS* **379**(2), 401–417 (2007) <https://arxiv.org/abs/astro-ph/0703531> [astro-ph]. <https://doi.org/10.1111/j.1365-2966.2007.11752.x>
- [33] Brough, S., van de Sande, J., Owers, M.S., d’Eugenio, F., Sharp, R., Cortese, L., Scott, N., Croom, S.M., Bassett, R., Bekki, K., Bland-Hawthorn, J., Bryant, J.J., Davies, R., Drinkwater, M.J., Driver, S.P., Foster, C., Goldstein, G., López-Sánchez, Á.R., Medling, A.M., Sweet, S.M., Taranu, D.S., Tonini, C., Yi, S.K., Goodwin, M., Lawrence, J.S., Richards, S.N.: The SAMI Galaxy Survey: Mass as the Driver of the Kinematic Morphology-Density Relation in Clusters. *ApJ* **844**(1), 59 (2017) <https://arxiv.org/abs/1704.01169> [astro-ph.GA]. <https://doi.org/10.3847/1538-4357/aa7a11>
- [34] Harborne, K.E., van de Sande, J., Cortese, L., Power, C., Robotham, A.S.G., Lagos, C.D.P., Croom, S.: Recovering λ_R and V/σ from seeing-dominated IFS data. *MNRAS* **497**(2), 2018–2038 (2020) <https://arxiv.org/abs/2006.12730> [astro-ph.GA]. <https://doi.org/10.1093/mnras/staa1847>
- [35] Trujillo, I., Cenarro, A.J., de Lorenzo-Cáceres, A., Vazdekis, A., de la Rosa, I.G., Cava, A.: Superdense Massive Galaxies in the Nearby Universe. *ApJ* **692**(2), 118–122 (2009) <https://arxiv.org/abs/0901.1032> [astro-ph.CO]. <https://doi.org/10.1088/0004-637X/692/2/L118>
- [36] Comerón, S., Trujillo, I., Cappellari, M., Buitrago, F., Garduño, L.E., Zaragoza-Cardiel, J., Zinchenko, I.A., Lara-López, M.A., Ferré-Mateu, A., Dib, S.: The massive relic galaxy NGC 1277 is dark matter deficient. From dynamical models of integral-field stellar kinematics out to five effective radii. *arXiv e-prints*, 2303–11360 (2023) <https://arxiv.org/abs/2303.11360> [astro-ph.GA]. <https://doi.org/10.48550/arXiv.2303.11360>
- [37] Naab, T., Johansson, P.H., Ostriker, J.P.: Minor Mergers and the Size Evolution of Elliptical Galaxies. *ApJ* **699**(2), 178–182 (2009) <https://arxiv.org/abs/0903.1636> [astro-ph.CO]. <https://doi.org/10.1088/0004-637X/699/2/L178>
- [38] Bezanson, R., van Dokkum, P.G., Tal, T., Marchesini, D., Kriek, M., Franx, M., Coppi, P.: The Relation Between Compact, Quiescent High-redshift Galaxies and Massive Nearby Elliptical Galaxies: Evidence for Hierarchical, Inside-Out Growth. *ApJ* **697**(2), 1290–1298 (2009) <https://arxiv.org/abs/0903.2044> [astro-ph.CO]. <https://doi.org/10.1088/0004-637X/697/2/1290>
- [39] Lagos, C.d.P., Stevens, A.R.H., Bower, R.G., Davis, T.A., Contreras, S., Padilla, N.D., Obreschkow, D., Croton, D., Trayford, J.W., Welker, C., Theuns, T.: Quantifying the impact of mergers on the angular momentum of simulated galaxies. *MNRAS* **473**(4), 4956–4974 (2018) <https://arxiv.org/abs/>

1701.04407 [astro-ph.GA]. <https://doi.org/10.1093/mnras/stx2667>

- [40] Lagos, C.d.P., Emsellem, E., van de Sande, J., Harborne, K.E., Cortese, L., Davison, T., Foster, C., Wright, R.J.: The diverse nature and formation paths of slow rotator galaxies in the EAGLE simulations. *MNRAS* **509**(3), 4372–4391 (2022) <https://arxiv.org/abs/2012.08060> [astro-ph.GA]. <https://doi.org/10.1093/mnras/stab3128>
- [41] Cappellari, M.: Structure and Kinematics of Early-Type Galaxies from Integral Field Spectroscopy. *ARA&A* **54**, 597–665 (2016) <https://arxiv.org/abs/1602.04267>. <https://doi.org/10.1146/annurev-astro-082214-122432>
- [42] Veale, M., Ma, C.-P., Greene, J.E., Thomas, J., Blakeslee, J.P., McConnell, N., Walsh, J.L., Ito, J.: The MASSIVE Survey - VII. The relationship of angular momentum, stellar mass and environment of early-type galaxies. *MNRAS* **471**(2), 1428–1445 (2017) <https://arxiv.org/abs/1703.08573> [astro-ph.GA]. <https://doi.org/10.1093/mnras/stx1639>
- [43] Tacconi, L.J., Genzel, R., Sternberg, A.: The Evolution of the Star-Forming Interstellar Medium Across Cosmic Time. *ARA&A* **58**, 157–203 (2020) <https://arxiv.org/abs/2003.06245> [astro-ph.GA]. <https://doi.org/10.1146/annurev-astro-082812-141034>
- [44] Smercina, A., Smith, J.-D.T., French, K.D., Bell, E.F., Dale, D.A., Medling, A.M., Nyland, K., Privon, G.C., Rowlands, K., Walter, F., Zabludoff, A.I.: After The Fall: Resolving the Molecular Gas in Post-starburst Galaxies. *ApJ* **929**(2), 154 (2022) <https://arxiv.org/abs/2108.03231> [astro-ph.GA]. <https://doi.org/10.3847/1538-4357/ac5d5f>
- [45] Venturi, G., Cresci, G., Marconi, A., Mingozi, M., Nardini, E., Carniani, S., Mannucci, F., Marasco, A., Maiolino, R., Perna, M., Treister, E., Bland-Hawthorn, J., Gallimore, J.: MAGNUM survey: Compact jets causing large turmoil in galaxies. Enhanced line widths perpendicular to radio jets as tracers of jet-ISM interaction. *A&A* **648**, 17 (2021) <https://arxiv.org/abs/2011.04677> [astro-ph.GA]. <https://doi.org/10.1051/0004-6361/202039869>
- [46] Böker, T., Arribas, S., Lützgendorf, N., Alves de Oliveira, C., Beck, T.L., Birkmann, S., Bunker, A.J., Charlot, S., de Marchi, G., Ferruit, P., Giardino, G., Jakobsen, P., Kumari, N., López-Caniego, M., Maiolino, R., Manjavacas, E., Marston, A., Moseley, S.H., Muzerolle, J., Ogle, P., Pirzkal, N., Rauscher, B., Rawle, T., Rix, H.-W., Sabbi, E., Sargent, B., Sirianni, M., te Plate, M., Valenti, J., Willott, C.J., Zeidler, P.: The Near-Infrared Spectrograph (NIR-Spec) on the James Webb Space Telescope. III. Integral-field spectroscopy. *A&A* **661**, 82 (2022) <https://arxiv.org/abs/2202.03308> [astro-ph.IM]. <https://doi.org/10.1051/0004-6361/202142589>
- [47] Jakobsen, P., Ferruit, P., Alves de Oliveira, C., Arribas, S., Bagnasco, G.,

- Barho, R., Beck, T.L., Birkmann, S., Böker, T., Bunker, A.J., Charlot, S., de Jong, P., de Marchi, G., Ehrenwinkler, R., Falcolini, M., Fels, R., Franx, M., Franz, D., Funke, M., Giardino, G., Gnata, X., Holota, W., Honnen, K., Jensen, P.L., Jentsch, M., Johnson, T., Jollet, D., Karl, H., Kling, G., Köhler, J., Kolm, M.-G., Kumari, N., Lander, M.E., Lemke, R., López-Caniego, M., Lützgendorf, N., Maiolino, R., Manjavacas, E., Marston, A., Maschmann, M., Maurer, R., Messerschmidt, B., Moseley, S.H., Mosner, P., Mott, D.B., Muzerolle, J., Pirzkal, N., Pittet, J.-F., Plitzke, A., Posselt, W., Rapp, B., Rauscher, B.J., Rawle, T., Rix, H.-W., Rödel, A., Rumler, P., Sabbi, E., Salvignol, J.-C., Schmid, T., Sirianni, M., Smith, C., Strada, P., te Plate, M., Valenti, J., Wettemann, T., Wiehe, T., Wiesmayer, M., Willott, C.J., Wright, R., Zeidler, P., Zincke, C.: The Near-Infrared Spectrograph (NIRSpec) on the James Webb Space Telescope. I. Overview of the instrument and its capabilities. *A&A* **661**, 80 (2022) <https://arxiv.org/abs/2202.03305> [astro-ph.IM]. <https://doi.org/10.1051/0004-6361/202142663>
- [48] Perna, M., Arribas, S., Marshall, M., D’Eugenio, F., Übler, H., Bunker, A., Charlot, S., Carniani, S., Jakobsen, P., Maiolino, R., Rodríguez Del Pino, B., Willott, C.J., Böker, T., Circosta, C., Cresci, G., Curti, M., Husemann, B., Kumari, N., Lamperti, I., Pérez-González, P.G., Scholtz, J.: The ultradense, interacting environment of a dual AGN at $z \sim 3.3$ revealed by JWST/NIRSpec IFS. arXiv e-prints, 2304–06756 (2023) <https://arxiv.org/abs/2304.06756> [astro-ph.GA]. <https://doi.org/10.48550/arXiv.2304.06756>
- [49] van Dokkum, P.G., Stanford, S.A.: The Fundamental Plane at $z=1.27$: First Calibration of the Mass Scale of Red Galaxies at Redshifts $z>1$. *ApJ* **585**(1), 78–89 (2003) <https://arxiv.org/abs/astro-ph/0210643> [astro-ph]. <https://doi.org/10.1086/345989>
- [50] Giavalisco, M., Ferguson, H.C., Koekemoer, A.M., Dickinson, M., Alexander, D.M., Bauer, F.E., Bergeron, J., Biagetti, C., Brandt, W.N., Casertano, S., Cesarsky, C., Chatzichristou, E., Conselice, C., Cristiani, S., Da Costa, L., Dahlen, T., de Mello, D., Eisenhardt, P., Erben, T., Fall, S.M., Fassnacht, C., Fosbury, R., Fruchter, A., Gardner, J.P., Grogin, N., Hook, R.N., Hornschemeier, A.E., Idzi, R., Jogee, S., Kretchmer, C., Laidler, V., Lee, K.S., Livio, M., Lucas, R., Madau, P., Mobasher, B., Moustakas, L.A., Nonino, M., Padovani, P., Papovich, C., Park, Y., Ravindranath, S., Renzini, A., Richardson, M., Riess, A., Rosati, P., Schirmer, M., Schreier, E., Somerville, R.S., Spinrad, H., Stern, D., Stiavelli, M., Strolger, L., Urry, C.M., Vandame, B., Williams, R., Wolf, C.: The Great Observatories Origins Deep Survey: Initial Results from Optical and Near-Infrared Imaging. *ApJ* **600**(2), 93–98 (2004) <https://arxiv.org/abs/astro-ph/0309105> [astro-ph]. <https://doi.org/10.1086/379232>
- [51] Illingworth, G., Magee, D., Bouwens, R., Oesch, P., Labbe, I., van Dokkum, P., Whitaker, K., Holden, B., Franx, M., Gonzalez, V.: The Hubble Legacy

- Fields (HLF-GOODS-S) v1.5 Data Products: Combining 2442 Orbits of GOODS-S/CDF-S Region ACS and WFC3/IR Images. arXiv e-prints, 1606–00841 (2016) <https://arxiv.org/abs/1606.00841> [astro-ph.GA]. <https://doi.org/10.48550/arXiv.1606.00841>
- [52] Grogin, N.A., Kocevski, D.D., Faber, S.M., Ferguson, H.C., Koekemoer, A.M., Riess, A.G., Acquaviva, V., Alexander, D.M., Almaini, O., Ashby, M.L.N., Barden, M., Bell, E.F., Bournaud, F., Brown, T.M., Caputi, K.I., Casertano, S., Cassata, P., Castellano, M., Challis, P., Chary, R.-R., Cheung, E., Cirasuolo, M., Conselice, C.J., Roshan Cooray, A., Croton, D.J., Daddi, E., Dahlen, T., Davé, R., de Mello, D.F., Dekel, A., Dickinson, M., Dolch, T., Donley, J.L., Dunlop, J.S., Dutton, A.A., Elbaz, D., Fazio, G.G., Filippenko, A.V., Finkelstein, S.L., Fontana, A., Gardner, J.P., Garnavich, P.M., Gawiser, E., Giavalisco, M., Grazian, A., Guo, Y., Hathi, N.P., Häussler, B., Hopkins, P.F., Huang, J.-S., Huang, K.-H., Jha, S.W., Kartaltepe, J.S., Kirshner, R.P., Koo, D.C., Lai, K., Lee, K.-S., Li, W., Lotz, J.M., Lucas, R.A., Madau, P., McCarthy, P.J., McGrath, E.J., McIntosh, D.H., McLure, R.J., Mobasher, B., Moustakas, L.A., Mozena, M., Nandra, K., Newman, J.A., Niemi, S.-M., Noeske, K.G., Papovich, C.J., Pentericci, L., Pope, A., Primack, J.R., Rajan, A., Ravindranath, S., Reddy, N.A., Renzini, A., Rix, H.-W., Robaina, A.R., Rodney, S.A., Rosario, D.J., Rosati, P., Salimbeni, S., Scarlata, C., Siana, B., Simard, L., Smidt, J., Somerville, R.S., Spinrad, H., Straughn, A.N., Strolger, L.-G., Telford, O., Teplitz, H.I., Trump, J.R., van der Wel, A., Villforth, C., Wechsler, R.H., Weiner, B.J., Wiklind, T., Wild, V., Wilson, G., Wuyts, S., Yan, H.-J., Yun, M.S.: CANDELS: The Cosmic Assembly Near-infrared Deep Extragalactic Legacy Survey. *ApJS* **197**(2), 35 (2011) <https://arxiv.org/abs/1105.3753> [astro-ph.CO]. <https://doi.org/10.1088/0067-0049/197/2/35>
- [53] Whitaker, K.E., Ashas, M., Illingworth, G., Magee, D., Leja, J., Oesch, P., van Dokkum, P., Mowla, L., Bouwens, R., Franx, M., Holden, B., Labbé, I., Rafelski, M., Teplitz, H., Gonzalez, V.: The Hubble Legacy Field GOODS-S Photometric Catalog. *ApJS* **244**(1), 16 (2019) <https://arxiv.org/abs/1908.05682> [astro-ph.GA]. <https://doi.org/10.3847/1538-4365/ab3853>
- [54] Cappellari, M., Emsellem, E.: Parametric Recovery of Line-of-Sight Velocity Distributions from Absorption-Line Spectra of Galaxies via Penalized Likelihood. *PASP* **116**, 138–147 (2004) <https://arxiv.org/abs/astro-ph/0312201>. <https://doi.org/10.1086/381875>
- [55] Foreman-Mackey, D., Hogg, D.W., Lang, D., Goodman, J.: emcee: The MCMC Hammer. *PASP* **125**, 306 (2013) <https://arxiv.org/abs/1202.3665> [astro-ph.IM]. <https://doi.org/10.1086/670067>
- [56] Übler, H., Maiolino, R., Curtis-Lake, E., Pérez-González, P.G., Curti, M., Perna, M., Arribas, S., Charlot, S., Marshall, M.A., D’Eugenio, F., Scholtz, J., Bunker, A., Carniani, S., Ferruit, P., Jakobsen, P., Rix, H.-W., Rodríguez Del

- Pino, B., Willott, C.J., Böker, T., Cresci, G., Jones, G.C., Kumari, N., Rawle, T.: GA-NIFS: A massive black hole in a low-metallicity AGN at $z \sim 5.55$ revealed by JWST/NIRSpec IFS. arXiv e-prints, 2302–06647 (2023) <https://arxiv.org/abs/2302.06647> [astro-ph.GA]. <https://doi.org/10.48550/arXiv.2302.06647>
- [57] Pérez-González, P.G., Barro, G., Annunziatella, M., Costantin, L., García-Argumánez, Á., McGrath, E.J., Mérida, R.M., Zavala, J.A., Haro, P.A., Bagley, M.B., Backhaus, B.E., Behroozi, P., Bell, E.F., Bisigello, L., Buat, V., Calabrò, A., Casey, C.M., Cleri, N.J., Coogan, R.T., Cooper, M.C., Cooray, A.R., Dekel, A., Dickinson, M., Elbaz, D., Ferguson, H.C., Finkelstein, S.L., Fontana, A., Franco, M., Gardner, J.P., Giavalisco, M., Gómez-Guijarro, C., Grazian, A., Grogin, N.A., Guo, Y., Huertas-Company, M., Joglee, S., Kartaltepe, J.S., Kewley, L.J., Kirkpatrick, A., Kocevski, D.D., Koekemoer, A.M., Long, A.S., Lotz, J.M., Lucas, R.A., Papovich, C., Pirzkal, N., Ravindranath, S., Somerville, R.S., Tacchella, S., Trump, J.R., Wang, W., Wilkins, S.M., Wuyts, S., Yang, G., Yung, L.Y.A.: CEERS Key Paper. IV. A Triality in the Nature of HST-dark Galaxies. *ApJ* **946**(1), 16 (2023) <https://arxiv.org/abs/2211.00045> [astro-ph.GA]. <https://doi.org/10.3847/2041-8213/acb3a5>
- [58] Bruzual, G., Charlot, S.: Stellar population synthesis at the resolution of 2003. *MNRAS* **344**, 1000–1028 (2003) <https://arxiv.org/abs/astro-ph/0309134>. <https://doi.org/10.1046/j.1365-8711.2003.06897.x>
- [59] Pérez-González, P.G., Gil de Paz, A., Zamorano, J., Gallego, J., Alonso-Herrero, A., Aragón-Salamanca, A.: Stellar populations in local star-forming galaxies - I. Data and modelling procedure. *MNRAS* **338**(2), 508–524 (2003) <https://arxiv.org/abs/astro-ph/0209396> [astro-ph]. <https://doi.org/10.1046/j.1365-8711.2003.06077.x>
- [60] Pérez-González, P.G., Rieke, G.H., Villar, V., Barro, G., Blaylock, M., Egami, E., Gallego, J., Gil de Paz, A., Pascual, S., Zamorano, J., Donley, J.L.: The Stellar Mass Assembly of Galaxies from $z = 0$ to $z = 4$: Analysis of a Sample Selected in the Rest-Frame Near-Infrared with Spitzer. *ApJ* **675**(1), 234–261 (2008) <https://arxiv.org/abs/0709.1354> [astro-ph]. <https://doi.org/10.1086/523690>
- [61] Calzetti, D., Armus, L., Bohlin, R.C., Kinney, A.L., Koornneef, J., Storchi-Bergmann, T.: The Dust Content and Opacity of Actively Star-forming Galaxies. *ApJ* **533**(2), 682–695 (2000) <https://arxiv.org/abs/astro-ph/9911459> [astro-ph]. <https://doi.org/10.1086/308692>
- [62] Domínguez Sánchez, H., Pérez-González, P.G., Esquej, P., Eliche-Moral, M.C., Barro, G., Cava, A., Koekemoer, A.M., Alcalde Pampliega, B., Alonso Herrero, A., Bruzual, G., Cardiel, N., Cenarro, J., Ceverino, D., Charlot, S., Hernán Caballero, A.: Pathways to quiescence: SHARDS view on the star

- formation histories of massive quiescent galaxies at $1.0 < z < 1.5$. *MNRAS* **457**(4), 3743–3768 (2016) <https://arxiv.org/abs/1507.07938> [astro-ph.GA]. <https://doi.org/10.1093/mnras/stw201>
- [63] Merlin, E., Castellano, M., Santini, P., Cipolletta, G., Boutsia, K., Schreiber, C., Buitrago, F., Fontana, A., Elbaz, D., Dunlop, J., Grazian, A., McLure, R., McLeod, D., Nonino, M., Milvang-Jensen, B., Derriere, S., Hathi, N.P., Pentericci, L., Fortuni, F., Calabrò, A.: The ASTRODEEP-GS43 catalogue: New photometry and redshifts for the CANDELS GOODS-South field. *A&A* **649**, 22 (2021) <https://arxiv.org/abs/2103.09246> [astro-ph.GA]. <https://doi.org/10.1051/0004-6361/202140310>
- [64] Shirley, R., Duncan, K., Campos Varillas, M.C., Hurley, P.D., Małek, K., Roehlly, Y., Smith, M.W.L., Aussel, H., Bakx, T., Buat, V., Burgarella, D., Christopher, N., Duivenvoorden, S., Eales, S., Efstathiou, A., González Solares, E.A., Griffin, M., Jarvis, M., Faro, B.L., Marchetti, L., McCheyney, I., Papadopoulos, A., Penner, K., Pons, E., Prescott, M., Rigby, E., Rottgering, H., Saxena, A., Scudder, J., Vaccari, M., Wang, L., Oliver, S.J.: HELP: the Herschel Extragalactic Legacy Project. *MNRAS* **507**(1), 129–155 (2021) <https://arxiv.org/abs/2105.05659> [astro-ph.GA]. <https://doi.org/10.1093/mnras/stab1526>
- [65] Boquien, M., Burgarella, D., Roehlly, Y., Buat, V., Ciesla, L., Corre, D., Inoue, A.K., Salas, H.: CIGALE: a python Code Investigating GALaxy Emission. *A&A* **622**, 103 (2019) <https://arxiv.org/abs/1811.03094> [astro-ph.GA]. <https://doi.org/10.1051/0004-6361/201834156>
- [66] Chabrier, G.: Galactic Stellar and Substellar Initial Mass Function. *PASP* **115**, 763–795 (2003) <https://arxiv.org/abs/astro-ph/0304382>. <https://doi.org/10.1086/376392>
- [67] Calzetti, D., Armus, L., Bohlin, R.C., Kinney, A.L., Koornneef, J., Storchi-Bergmann, T.: The Dust Content and Opacity of Actively Star-forming Galaxies. *ApJ* **533**(2), 682–695 (2000) <https://arxiv.org/abs/astro-ph/9911459> [astro-ph]. <https://doi.org/10.1086/308692>
- [68] Dale, D.A., Helou, G., Magdis, G.E., Armus, L., Díaz-Santos, T., Shi, Y.: A Two-parameter Model for the Infrared/Submillimeter/Radio Spectral Energy Distributions of Galaxies and Active Galactic Nuclei. *ApJ* **784**(1), 83 (2014) <https://arxiv.org/abs/1402.1495> [astro-ph.GA]. <https://doi.org/10.1088/0004-637X/784/1/83>
- [69] Fritz, J., Franceschini, A., Hatziminaoglou, E.: Revisiting the infrared spectra of active galactic nuclei with a new torus emission model. *MNRAS* **366**(3), 767–786 (2006) <https://arxiv.org/abs/astro-ph/0511428> [astro-ph]. <https://doi.org/10.1111/j.1365-2966.2006.09866.x>

- [70] Circosta, C., Mainieri, V., Padovani, P., Lanzuisi, G., Salvato, M., Harrison, C.M., Kakkad, D., Puglisi, A., Vietri, G., Zamorani, G., Cicone, C., Husemann, B., Vignali, C., Balmaverde, B., Bischetti, M., Bongiorno, A., Brusa, M., Carniani, S., Civano, F., Comastri, A., Cresci, G., Feruglio, C., Fiore, F., Fotopoulou, S., Karim, A., Lamastra, A., Magnelli, B., Mannucci, F., Marconi, A., Merloni, A., Netzer, H., Perna, M., Piconcelli, E., Rodighiero, G., Schinnerer, E., Schramm, M., Schulze, A., Silverman, J., Zappacosta, L.: SUPER. I. Toward an unbiased study of ionized outflows in $z \sim 2$ active galactic nuclei: survey overview and sample characterization. *A&A* **620**, 82 (2018) <https://arxiv.org/abs/1809.04858> [astro-ph.GA]. <https://doi.org/10.1051/0004-6361/201833520>
- [71] Cappellari, M.: Improving the full spectrum fitting method: accurate convolution with Gauss-Hermite functions. *MNRAS* **466**(1), 798–811 (2017) <https://arxiv.org/abs/1607.08538> [astro-ph.GA]. <https://doi.org/10.1093/mnras/stw3020>
- [72] Cappellari, M.: Full spectrum fitting with photometry in ppxf: non-parametric star formation history, metallicity and the quenching boundary from 3200 LEGA-C galaxies at redshift $z \sim 0.8$. arXiv e-prints, 2208–14974 (2022) <https://arxiv.org/abs/2208.14974> [astro-ph.GA]
- [73] Choi, J., Dotter, A., Conroy, C., Cantiello, M., Paxton, B., Johnson, B.D.: Mesa Isochrones and Stellar Tracks (MIST). I. Solar-scaled Models. *ApJ* **823**(2), 102 (2016) <https://arxiv.org/abs/1604.08592> [astro-ph.SR]. <https://doi.org/10.3847/0004-637X/823/2/102>
- [74] Conroy, C., Naidu, R.P., Zaritsky, D., Bonaca, A., Cargile, P., Johnson, B.D., Caldwell, N.: Resolving the Metallicity Distribution of the Stellar Halo with the H3 Survey. *ApJ* **887**(2), 237 (2019) <https://arxiv.org/abs/1909.02007> [astro-ph.GA]. <https://doi.org/10.3847/1538-4357/ab5710>
- [75] van de Sande, J., Bland-Hawthorn, J., Fogarty, L.M.R., Cortese, L., d’Eugenio, F., Croom, S.M., Scott, N., Allen, J.T., Brough, S., Bryant, J.J., Cecil, G., Colless, M., Couch, W.J., Davies, R., Elahi, P.J., Foster, C., Goldstein, G., Goodwin, M., Groves, B., Ho, I.-T., Jeong, H., Jones, D.H., Konstantopoulos, I.S., Lawrence, J.S., Leslie, S.K., López-Sánchez, Á.R., McDermid, R.M., McElroy, R., Medling, A.M., Oh, S., Owers, M.S., Richards, S.N., Schaefer, A.L., Sharp, R., Sweet, S.M., Taranu, D., Tonini, C., Walcher, C.J., Yi, S.K.: The SAMI Galaxy Survey: Revisiting Galaxy Classification through High-order Stellar Kinematics. *ApJ* **835**, 104 (2017) <https://arxiv.org/abs/1611.07039>. <https://doi.org/10.3847/1538-4357/835/1/104>
- [76] Kewley, L.J., Nicholls, D.C., Sutherland, R., Rigby, J.R., Acharya, A., Dopita, M.A., Bayliss, M.B.: Theoretical ISM Pressure and Electron Density Diagnostics for Local and High-redshift Galaxies. *ApJ* **880**(1), 16 (2019) <https://>

- arxiv.org/abs/1908.05504 [astro-ph.GA]. <https://doi.org/10.3847/1538-4357/ab16ed>
- [77] Poznanski, D., Prochaska, J.X., Bloom, J.S.: An empirical relation between sodium absorption and dust extinction. *MNRAS* **426**(2), 1465–1474 (2012) <https://arxiv.org/abs/1206.6107> [astro-ph.IM]. <https://doi.org/10.1111/j.1365-2966.2012.21796.x>
- [78] Worthey, G.: Comprehensive stellar population models and the disentanglement of age and metallicity effects. *ApJS* **95**, 107–149 (1994). <https://doi.org/10.1086/192096>
- [79] Wu, P.-F., van der Wel, A., Bezanson, R., Gallazzi, A., Pacifici, C., Straatman, C.M.S., Barišić, I., Bell, E.F., Chauke, P., D’Eugenio, F., Franx, M., Muzzin, A., Sobral, D., van Houdt, J.: The Colors and Sizes of Recently Quenched Galaxies: A Result of Compact Starburst before Quenching. *ApJ* **888**(2), 77 (2020) <https://arxiv.org/abs/1912.03683> [astro-ph.GA]. <https://doi.org/10.3847/1538-4357/ab5fd9>
- [80] Cappellari, M., Copin, Y.: Adaptive spatial binning of integral-field spectroscopic data using Voronoi tessellations. *MNRAS* **342**(2), 345–354 (2003) <https://arxiv.org/abs/astro-ph/0302262> [astro-ph]. <https://doi.org/10.1046/j.1365-8711.2003.06541.x>
- [81] Foster, C., Mendel, J.T., Lagos, C.D.P., Wisnioski, E., Yuan, T., D’Eugenio, F., Barone, T.M., Harborne, K.E., Vaughan, S.P., Schulze, F., Remus, R.-S., Gupta, A., Collacchioni, F., Khim, D.J., Taylor, P., Bassett, R., Croom, S.M., McDermid, R.M., Poci, A., Battisti, A.J., Bland-Hawthorn, J., Bellstedt, S., Colless, M., Davies, L.J.M., Derkenne, C., Driver, S., Ferré-Mateu, A., Fisher, D.B., Gjergo, E., Johnston, E.J., Khalid, A., Kobayashi, C., Oh, S., Peng, Y., Robotham, A.S.G., Sharda, P., Sweet, S.M., Taylor, E.N., Tran, K.-V.H., Trayford, J.W., van de Sande, J., Yi, S.K., Zanisi, L.: The MAGPI survey: Science goals, design, observing strategy, early results and theoretical framework. *Publ. Astron. Soc. Australia* **38**, 031 (2021) <https://arxiv.org/abs/2011.13567> [astro-ph.GA]. <https://doi.org/10.1017/pasa.2021.25>
- [82] Schwarz, G.: Estimating the Dimension of a Model. *The Annals of Statistics* **6**(2), 461–464 (1978). <https://doi.org/10.1214/aos/1176344136>
- [83] Carniani, S., Marconi, A., Maiolino, R., Balmaverde, B., Brusa, M., Cano-Díaz, M., Cicone, C., Comastri, A., Cresci, G., Fiore, F., Feruglio, C., La Franca, F., Mainieri, V., Mannucci, F., Nagao, T., Netzer, H., Piconcelli, E., Risaliti, G., Schneider, R., Shemmer, O.: Ionised outflows in $z \sim 2.4$ quasar host galaxies. *A&A* **580**, 102 (2015) <https://arxiv.org/abs/1506.03096> [astro-ph.GA]. <https://doi.org/10.1051/0004-6361/201526557>
- [84] Kakkad, D., Sani, E., Rojas, A.F., Mallmann, N.D., Veilleux, S., Bauer, F.E.,

- Ricci, F., Mushotzky, R., Koss, M., Ricci, C., Treister, E., Privon, G.C., Nguyen, N., Bär, R., Harrison, F., Oh, K., Powell, M., Riffel, R., Stern, D., Trakhtenbrot, B., Urry, C.M.: BASS XXXI: Outflow scaling relations in low redshift X-ray AGN host galaxies with MUSE. *MNRAS* **511**(2), 2105–2124 (2022) <https://arxiv.org/abs/2201.04149> [astro-ph.GA]. <https://doi.org/10.1093/mnras/stac103>
- [85] Fiore, F., Feruglio, C., Shankar, F., Bischetti, M., Bongiorno, A., Brusa, M., Carniani, S., Cicone, C., Duras, F., Lamastra, A., Mainieri, V., Marconi, A., Menci, N., Maiolino, R., Piconcelli, E., Vietri, G., Zappacosta, L.: AGN wind scaling relations and the co-evolution of black holes and galaxies. *A&A* **601**, 143 (2017) <https://arxiv.org/abs/1702.04507> [astro-ph.GA]. <https://doi.org/10.1051/0004-6361/201629478>
- [86] Harrison, C.M., Alexander, D.M., Mullaney, J.R., Stott, J.P., Swinbank, A.M., Arumugam, V., Bauer, F.E., Bower, R.G., Bunker, A.J., Sharples, R.M.: The KMOS AGN Survey at High redshift (KASHz): the prevalence and drivers of ionized outflows in the host galaxies of X-ray AGN. *MNRAS* **456**(2), 1195–1220 (2016) <https://arxiv.org/abs/1511.00008> [astro-ph.GA]. <https://doi.org/10.1093/mnras/stv2727>
- [87] Baron, D., Netzer, H.: Discovering AGN-driven winds through their infrared emission - II. Mass outflow rate and energetics. *MNRAS* **486**(3), 4290–4303 (2019) <https://arxiv.org/abs/1903.11076> [astro-ph.GA]. <https://doi.org/10.1093/mnras/stz1070>
- [88] Davies, R., Baron, D., Shimizu, T., Netzer, H., Burtscher, L., de Zeeuw, P.T., Genzel, R., Hicks, E.K.S., Koss, M., Lin, M.-Y., Lutz, D., Maciejewski, W., Müller-Sánchez, F., Orban de Xivry, G., Ricci, C., Riffel, R., Riffel, R.A., Rosario, D., Schartmann, M., Schnorr-Müller, A., Shangguan, J., Sternberg, A., Sturm, E., Storchi-Bergmann, T., Tacconi, L., Veilleux, S.: Ionized outflows in local luminous AGN: what are the real densities and outflow rates? *MNRAS* **498**(3), 4150–4177 (2020) <https://arxiv.org/abs/2003.06153> [astro-ph.GA]. <https://doi.org/10.1093/mnras/staa2413>
- [89] Cazzoli, S., Arribas, S., Maiolino, R., Colina, L.: Neutral gas outflows in nearby [U]LIRGs via optical NaD feature. *A&A* **590**, 125 (2016) <https://arxiv.org/abs/1602.08505> [astro-ph.GA]. <https://doi.org/10.1051/0004-6361/201526788>
- [90] Rupke, D.S., Veilleux, S., Sanders, D.B.: Outflows in Infrared-Luminous Starbursts at $z < 0.5$. II. Analysis and Discussion. *ApJS* **160**(1), 115–148 (2005) <https://arxiv.org/abs/astro-ph/0506611> [astro-ph]. <https://doi.org/10.1086/432889>
- [91] Maiolino, R., Gallerani, S., Neri, R., Cicone, C., Ferrara, A., Genzel, R., Lutz, D., Sturm, E., Tacconi, L.J., Walter, F., Feruglio, C., Fiore, F., Piconcelli, E.:

- Evidence of strong quasar feedback in the early Universe. *MNRAS* **425**(1), 66–70 (2012) <https://arxiv.org/abs/1204.2904> [astro-ph.CO]. <https://doi.org/10.1111/j.1745-3933.2012.01303.x>
- [92] Veilleux, S., Cecil, G., Bland-Hawthorn, J.: Galactic Winds. *ARA&A* **43**(1), 769–826 (2005) <https://arxiv.org/abs/astro-ph/0504435> [astro-ph]. <https://doi.org/10.1146/annurev.astro.43.072103.150610>
- [93] Arribas, S., Colina, L., Bellocchi, E., Maiolino, R., Villar-Martín, M.: Ionized gas outflows and global kinematics of low-*z* luminous star-forming galaxies. *A&A* **568**, 14 (2014) <https://arxiv.org/abs/1404.1082> [astro-ph.GA]. <https://doi.org/10.1051/0004-6361/201323324>
- [94] van Rossum, G.: Python tutorial. CWI Technical Report **CS-R9526** (1995)
- [95] Astropy Collaboration, Robitaille, T.P., Tollerud, E.J., Greenfield, P., Droettboom, M., Bray, E., Aldcroft, T., Davis, M., Ginsburg, A., Price-Whelan, A.M., Kerzendorf, W.E., Conley, A., Crighton, N., Barbary, K., Muna, D., Ferguson, H., Grollier, F., Parikh, M.M., Nair, P.H., Unther, H.M., Deil, C., Woillez, J., Conseil, S., Kramer, R., Turner, J.E.H., Singer, L., Fox, R., Weaver, B.A., Zabalza, V., Edwards, Z.I., Azalee Bostroem, K., Burke, D.J., Casey, A.R., Crawford, S.M., Dencheva, N., Ely, J., Jenness, T., Labrie, K., Lim, P.L., Pierfederici, F., Pontzen, A., Ptak, A., Refsdal, B., Servillat, M., Streicher, O.: Astropy: A community Python package for astronomy. *A&A* **558**, 33 (2013) <https://arxiv.org/abs/1307.6212> [astro-ph.IM]. <https://doi.org/10.1051/0004-6361/201322068>
- [96] Speagle, J.S.: DYNESTY: a dynamic nested sampling package for estimating Bayesian posteriors and evidences. *MNRAS* **493**(3), 3132–3158 (2020) <https://arxiv.org/abs/1904.02180> [astro-ph.IM]. <https://doi.org/10.1093/mnras/staa278>
- [97] Conroy, C., Gunn, J.E., White, M.: The Propagation of Uncertainties in Stellar Population Synthesis Modeling. I. The Relevance of Uncertain Aspects of Stellar Evolution and the Initial Mass Function to the Derived Physical Properties of Galaxies. *ApJ* **699**(1), 486–506 (2009) <https://arxiv.org/abs/0809.4261> [astro-ph]. <https://doi.org/10.1088/0004-637X/699/1/486>
- [98] Conroy, C., Gunn, J.E.: FSPS: Flexible Stellar Population Synthesis. *Astrophysics Source Code Library*, record ascl:1010.043 (2010)
- [99] Hunter, J.D.: Matplotlib: A 2D Graphics Environment. *Computing in Science and Engineering* **9**(3), 90–95 (2007). <https://doi.org/10.1109/MCSE.2007.55>
- [100] Harris, C.R., Millman, K.J., van der Walt, S.J., Gommers, R., Virtanen, P., Cournapeau, D., Wieser, E., Taylor, J., Berg, S., Smith, N.J., Kern, R., Picus, M., Hoyer, S., van Kerkwijk, M.H., Brett, M., Haldane, A., del Río,

- J.F., Wiebe, M., Peterson, P., Gérard-Marchant, P., Sheppard, K., Reddy, T., Weckesser, W., Abbasi, H., Gohlke, C., Oliphant, T.E.: Array programming with NumPy. *Nature* **585**(7825), 357–362 (2020) <https://arxiv.org/abs/2006.10256> [cs.MS]. <https://doi.org/10.1038/s41586-020-2649-2>
- [101] Johnson, B.D., Leja, J., Conroy, C., Speagle, J.S.: Stellar Population Inference with Prospector. *ApJS* **254**(2), 22 (2021) <https://arxiv.org/abs/2012.01426> [astro-ph.GA]. <https://doi.org/10.3847/1538-4365/abef67>
- [102] Johnson, B., Foreman-Mackey, D., Sick, J., Leja, J., Byler, N., Walmsley, M., Tollerud, E., Leung, H., Scott, S., Park, M.: Dfm/python-fsps: V0.4.4. <https://doi.org/10.5281/zenodo.8230430>. <https://doi.org/10.5281/zenodo.8230430>
- [103] Jones, E., Oliphant, T., Peterson, P., et al.: SciPy: Open source scientific tools for Python. [Online; accessed <today>] (2001). <http://www.scipy.org/>